

CHARACTERIZATION AND MODELING OF
FERROMAGNETIC SHAPE MEMORY NIMNGA
ACTUATORS

DISSERTATION

Presented in Partial Fulfillment of the Requirements for
the Degree Doctor of Philosophy in the
Graduate School of The Ohio State University

By

Xiang Wang, B.S.

* * * * *

The Ohio State University

2008

Dissertation Committee:

Marcelo Dapino, Adviser

Stephen Bechtel

Mark Walter

Gregory Washington

Approved by

Adviser

Graduate Program in
Mechanical Engineering

© Copyright by

Xiang Wang

2008

ABSTRACT

It has been shown that a magnetic field induced strain (MFIS) up to 10 % can be obtained when Ferromagnetic Shape Memory Alloys (FSMAs) in the NiMnGa system are driven by perpendicular magnetic field and mechanical stresses. Prior experiments on single crystal $\text{Ni}_{50}\text{Mn}_{28.7}\text{Ga}_{21.3}$ have demonstrated the existence of reversible strains along the [001] crystallographic axis of a cylindrical rod under the application of collinear magnetic fields and stresses. This unusual behavior is used in this paper to develop a dynamic model for NiMnGa as operated in a solenoid transducer consisting of a driving coil and an external mass-spring-damper loading. A constitutive model to describe the motion of twin boundaries in the presence of energetically strong pinning sites is presented. The effective pinning strength is represented by an internal bias stress oriented transversely. This also explains the reduced maximum MFIS of -0.41% compared to possible -6% obtained from its variant structure. Stochastic homogenization is then used to account for variability in the bias stresses throughout the material and inhomogeneity in the interaction field intensity. Finally, the internal rod dynamics are modeled through force balancing with boundary conditions dictated by the constructive details of the transducer and mechanical

load. The model is formulated in variational form, resulting in a second-order temporal system with magnetic field induced strain as the driving mechanism. Model results are compared with experimental measurements for validation and parameter identification. To provide a theoretical understanding of the frequency-dependent power losses in NiMnGa, this dissertation also extends the constitutive hysteresis model by incorporating eddy current and magnetic domain configuration(anomalous) losses; the analytical solutions are compared with finite element simulations. Finally, a parametric analysis of NiMnGa actuator performance based on energy delivery efficiency and the energy conversion efficiency is provided. The optimal stiffness ratios from the classical linear constitutive model and our nonlinear model are experimentally validated. The approach presented is useful for designing a control system, especially for the purpose of designing an energy efficient control system.

ACKNOWLEDGMENTS

First, I would like to take this opportunity to gratefully and sincerely thank my advisor, Prof. Marcelo Dapino. He was patient with me when I first got into the field of smart materials and structures, and he has always been enthusiastic to help me in my graduate studies. Without his understanding, support and encouragement, it would not be possible for me to finish the work in this dissertation. His guidance and enthusiasm through all these years are greatly appreciated. My great appreciations extend to Prof. Bechtel, Prof. Washington and Prof. Walter for being in my committee and their valuable advices and time.

I would also like to thank my colleagues, Philip for proofreading my papers, and Neelesh for the instructive discussion in research, and all other members in SMSL lab maintaining the team work environment which makes the research an enjoyable experience.

Words can not express my indebtedness to my parents for their constant patience and encouragements during my life. It would be impossible to overcome all the difficulties and finish this work without their support. Last but not least, I would like to express my deep gratitude to my wife Yiwen, I really appreciate your incredible

and continuous sacrifices. Your understanding and encouragement always gave me a huge momentum to continue my work.

VITA

July 13, 1977 Born - Yangzhou, China

1994-1998 B.S. Huazhong University of Science
and Technology

2001-2003 University of Arizona

2003-present Graduate Research Assistant,
Ohio State University.

PUBLICATIONS

Research Publications

Wang X., and Dapino M. “Model for the magnetomechanical behavior of NiMnGa driven with collinear field and stress”. *Proceedings of SPIE Smart Structures and Materials Conference*, 6170, 2006.

Wang X., and Dapino M. “Dynamic modeling and characterization of ferromagnetic shape memory NiMnGa”. *Proceedings of ASME International Mechanical Engineering Congress and Exposition*, IMECE2007-43713, 2007.

FIELDS OF STUDY

Major Field: Mechanical Engineering

TABLE OF CONTENTS

	Page
Abstract	ii
Acknowledgments	iv
Vita	vi
List of Tables	x
List of Figures	xi
Chapters:	
1. INTRODUCTION	1
1.1 Dissertation Overview	1
1.2 Dissertation Organization	5
2. FERROMAGNETIC SHAPE MEMORY ALLOYS	7
2.1 Twin Variant Structure	8
2.2 Strain Mechanism	10
2.2.1 Modeling Literature Review	14
3. CONSTITUTIVE MODEL	18
3.1 Formulation of Gibbs Free Energy	19
3.2 Evolution of the Reorientation Strain	23
3.3 Stochastic Homogenization Method	26

4.	TRANSDUCER MODEL	28
4.1	Solenoid Based Transducer	28
4.2	Strong and Weak Form	29
4.2.1	Strong Form	30
4.2.2	Weak Form	33
4.3	Numerical Approximation	33
4.3.1	Galerkin Discretization	33
4.3.2	Trapezoidal Method	35
4.4	Experiments and Results	36
4.4.1	Parameter Identification	37
4.4.2	Stochastic Homogenization Implementation	39
4.4.3	Model Results	43
5.	POWER LOSSES AND MAGNETIC FIELD DIFFUSION	45
5.1	Background	45
5.1.1	Eddy Currents	45
5.1.2	Eddy Current Power Loss Literature Review	47
5.2	Hysteresis Model With Eddy Current Loss	48
5.3	Skin Depth Effect	53
5.3.1	Diffusion Equation	53
5.3.2	Finite Element Analysis	56
6.	EFFICIENCY ANALYSIS	67
6.1	Introduction	67
6.2	Analytical Approach	68
6.2.1	Definitions	69
6.2.2	Analytic Expressions	70
6.3	Experimental Validation	74
6.3.1	Coil Characterization	75
6.3.2	Actuation Test	77
7.	CONCLUSIONS AND FUTURE WORK	81
7.1	Conclusions	81
7.2	Future Work	83

Appendices:

A.	EFFICIENCY TEST DEVICE DRAWINGS	84
B.	FIELD INDUCED STRAIN VERSUS CURRENT	93
C.	CODE	94
	C.1 Volume Fraction Evolution Function	94
	C.2 Piecewise Stress-Strain Fitting Function	94
	C.3 Constrained Optimization Function	96
	C.4 Mean Square Error Calculating Function	96
	C.5 Legendre Points and Weights Calculating Function	97
	C.6 Kernel Calculating Function	97
	C.7 Transducer Structure Matrix Generating Function	98
	C.8 Transducer Deformation Calculating Function	99
	C.9 Parametric Efficiency Analysis Function	101
	Bibliography	105

LIST OF TABLES

Table		Page
3.1	Index convention in tensor notation	22
4.1	Model parameters identified from experimental data.	38
4.2	4-point Gaussian quadrature points and weights	42
4.3	Model parameter values.	43
4.4	Model parameter values.	44
5.1	Error at different locations between analytic result and COMSOL re- sult for samples with different lengths	65
6.1	Conversion and delivery efficiencies for springs with different stiffness rates	79

LIST OF FIGURES

Figure		Page
1.1	NiMnGa drive configuration.	3
2.1	Maximum strain vs. maximum bandwidth for different smart materials.	8
2.2	Two-dimensional representation of field-induced twin-boundary motion.	9
2.3	(a) Twin and microstructure of 5M martensitic phase of NiMnGa obtained from in situ optical and magneto-optical observations. (b) Schematic representation of the twin structure.	10
2.4	Strain mechanism with perpendicular fields and stresses: (a) initial status with zero field and stress; (b) volume fraction change when applying magnetic field; (c) removal of external field; (d) restoring the sample with orthogonal mechanical stress.	11
2.5	Strain mechanism with collinear fields and stresses: (a) initial status with internal bias stress; (b)(c) volume fraction change with small and large axial magnetic field; (d) removal of external field.	15
3.1	Notation and orientation of the twin-variant structure assumed for model development.	20
4.1	(a) Solenoid based transducer; (b) schematic representation.	29
4.2	1-dimensional representation of NiMnGa transducer.	30
4.3	Infinitesimal element considered for force analysis.	31
4.4	experiment data	38

4.5	(a) Interaction field distribution. (b) Slope parameter distribution.	40
4.6	Kernels with different slopes.	40
4.7	result	44
5.1	Laminated cylindrical sample.	50
5.2	Simplified two-variant NiMnga microstructure incorporating internal state variables.	52
5.3	Schematic representation of the NiMnGa sample put in a magnetic field parallel to axial direction.	54
5.4	Skin depth effect.	56
5.5	Geometry of the model.	58
5.6	A magnetomechanical system.	59
5.7	Magnetic field distribution in one cycle.	63
5.8	Magnetic field at different locations from the center to the surface of the sample.	64
5.9	Comparison of magnetic field at different locations between COMSOL result and analytic result: (a) Sample length = 0.8 in. (b) Sample length = 8 in.	65
5.10	Comparison of field induced strain between the constitutive model and COMSOL with eddy current power loss.	66
6.1	experiment data	70
6.2	Experimental setup.	75
6.3	Impedance versus frequency in the coil characterization.	76
6.4	Stress-strain curve for AdaptaMat NiMnGa sample.	78

6.5	(a) Energy conversion efficiency; (b) Energy delivery efficiency	79
A.1	Fixture Side plates.	84
A.2	Prestress adjusting plate.	85
A.3	Bottom plate.	86
A.4	Push rod.	87
A.5	Bushing.	88
A.6	Fixture feet.	89
A.7	Sample grip.	90
A.8	Top plate.	91
A.9	Upper rod.	92
B.1	Field induced strain versus current.	93

CHAPTER 1

INTRODUCTION

1.1 Dissertation Overview

Ferromagnetic shape memory alloys in the nickel-manganese-gallium (NiMnGa) system are attractive for actuation and sensing applications; large bidirectional strains of up to 10% can be produced in these alloys by twin boundary motion as martensite variants rotate to align parallel or perpendicular to applied magnetic fields or stresses, respectively. Compared with other active materials, NiMnGa can potentially achieve both high bandwidth and large strains in response to magnetic fields. Other active materials, such as piezoceramic and magnetostrictive materials have higher frequency bandwidth, but they can produce only small strains on the order of 10^{-3} . Shape memory alloys can produce strains in excess of 8% in tension, but at the expense of slow responses due to the restriction of thermal dissipation.

In the Heusler alloy Ni₂MnGa, cooling below the characteristic martensite start temperature produces a cubic to tetragonal transformation and a corresponding twin-variant structure. Over a certain compositional range, a typical martensite

microstructure consists of a mixture of three variants, each with tetragonal lattice $c \times c \times a$ ($c/a=0.94$), in which adjacent variants are separated by a boundary known as a twin plane. Large magnetic field-induced strain results from the reorientation of favorable martensite variants through the motion of twin boundaries. Either magnetic fields or stresses can be used to transform the material to a single variant. Since both magnetic fields and compressive stresses favor alignment of the short c -axis of the tetragonal unit cell, in actuator applications a fixed stress oriented perpendicular to the drive field is usually applied to restore the twin variants and obtain reversible magnetic field induced strain when the drive field is cycled. This mechanism is implemented by placing a rectangular specimen in an electromagnet with the drive field applied along the $[110]$ direction and the load axis oriented along the $[001]$ direction (Fig. 1.1(a)) – both directions relative to the parent austenite phase. However, the electromagnets are usually very heavy and bulky, and the open magnetic circuit also makes this device have a low energy efficiency.

In prior experiments it has been established [39] that reversible strains of at least -0.41% are possible in single-crystal $\text{Ni}_{50}\text{Mn}_{28.7}\text{Ga}_{21.3}$ exposed to alternating magnetic fields along the $[001]$ direction of the parent austenite phase and no external restoring force. This result is significant because it enables solenoid-based NiMnGa transducers like that shown in Fig. 1.1(b), which by including a path for flux return are significantly more compact, lightweight and energy efficient than conventional

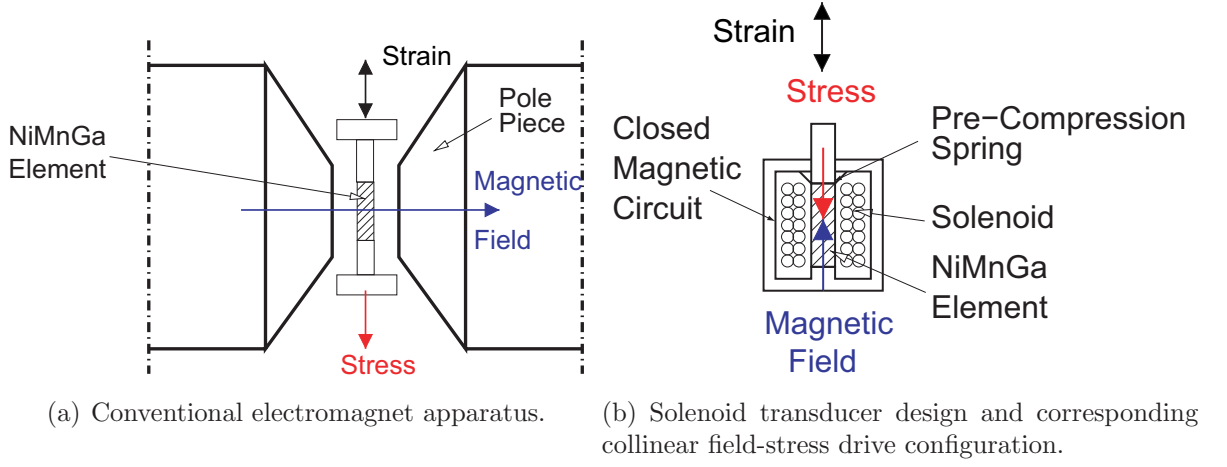


Figure 1.1: NiMnGa drive configuration.

electromagnet devices as that shown in Fig. 1.1(a). It is emphasized that the reversibility of the magnetic field induced strain observed in these experiments cannot be explained by existing models for martensitic variant reorientation, which are based on the competing effects of the stress energy and Zeeman energy as the latter attempts to overcome the twin boundary energy. This points to the existence of bias or residual stresses built into the material during crystal growth. The bias stresses are attributed to high-strength pinning sites or point defects which act as localized energy potentials that oppose twin boundary motion and provide an otherwise nonexistent restoring force when the magnetic field is removed. The presence of pinning sites also explains the reduced deformations relative to alloys capable of over 6% strain, in which twin boundary motion is largely unimpeded.

The above properties of the special solenoid-based transducer driven NiMnGa enable a high stroke and broad band actuator, the effective design and control of the actuator requires understanding of the mechanisms that govern the magnetic field induced strain and quantification of the relationship between applied fields, strains, and stresses in a transducer. Various constitutive models were proposed by many groups to quantitatively describe this relationship[34, 37, 32, 17, 47, 43, 27]. This dissertation formulates a model by considering the Zeeman, elastic, and pinning energies of a simplified two-variant structure in the presence of a magnetic fields and external stresses applied collinearly. The model also addresses the problem caused by the variability in the density and strength of the pinning sites throughout the material by considering stochastic homogenization, which has been proven accurate and efficient to implement as a design and control tool for ferroelectric, ferromagnetic, and shape memory materials [48]. The resulting constitutive model characterizes the magnetic field induced strain but does not account for the material dynamics created as the NiMnGa driver element vibrates and does work against an external mechanical load, which is critical for design and control purposes. To that end, a dynamic transducer model is formulated by considering a continuum plane-wave model for the NiMnGa rod and a single degree of freedom spring, mass and damper system for the external load. Force balancing yields a PDE system which is expressed in weak or variational form through a Galerkin discretization in space. This yields a second-order temporal

system in which the input is the force created through MFIS, and the output is the deflection at the end of the NiMnGa rod connected to the load.

The dissertation also extends the model from quasi-static to dynamic magnetic fields by incorporating the power losses for electrically conducting materials. The skin depth effects are also simulated in finite element analysis software.

To design an energy efficient control system, a parametric analysis of a NiMnGa based transducer is developed considering the efficiency of the energy delivered to the external load and the efficiency with which the transducer converts the input electrical energy into output mechanical energy. The nonlinear and linear constitutive models are applied to calculate the optimal stiffness ratio, which is validated by the experimental data.

1.2 Dissertation Organization

Chapter 2 provides a discussion of magnetostrictive, piezoelectric, and shape memory materials. For NiMnGa, the strain mechanisms for both the conventional (perpendicular) and the collinear stress-field configurations are discussed. A summary of the current literatures on NiMnGa modeling is also provided.

In Chapter 3, a detailed constitutive model for NiMnGa driven by a collinear magnetic field and mechanical stress along the axial direction is discussed. The accuracy of the model to describe the evolution of the reorientation strain is improved by applying stochastic homogenization. The model parameters are determined from

experimental data presented by Malla [39] and the model is compared with the experimental results.

Chapter 4 extends the model by considering a dynamic system composed of a NiMnGa sample working against an external mechanical load. Strong form and the weak form are derived with the system equations solved by the numerical discretization method.

Chapter 5 incorporates the power losses in the same manner as [30, 3], in which the dynamic loss is decomposed into three components. The results from the extended quasi-static constitutive model are compared with simulations obtained with the finite element package COMSOL.

In Chapter 6, definitions of energy delivery efficiency and energy conversion efficiency for a simplified NiMnGa transducer are provided. The parametric analysis of energy efficiency will give the optimal stiffness of the external spring load. A custom made actuator is designed to verify the theoretical results.

Finally, Chapter 7 concludes the dissertation and gives several suggestions for future work.

CHAPTER 2

FERROMAGNETIC SHAPE MEMORY ALLOYS

Smart materials can adapt to their environment by changing their material properties and shape in response to external stimuli. For example, piezoelectric materials produce an electric charge when subjected to stress and deform when subjected to an electric field; shape memory alloys (SMAs) undergo a crystallographic phase change and exhibit large deformations in response to a temperature change or mechanical loading, etc. Fig. 2.1 shows smart materials either provide high stroke such as SMAs, or fast response such as magnetostrictive and piezoelectric materials. The materials available for applications requiring both high stroke and high frequencies are limited. Ferromagnetic shape memory alloys can potentially provide the best of both worlds: large stroke in the percent range and fast response in the kHz range due to the magnetic activation. In this chapter, a detailed introduction of the properties of ferromagnetic shape memory alloys and research in this field are provided.

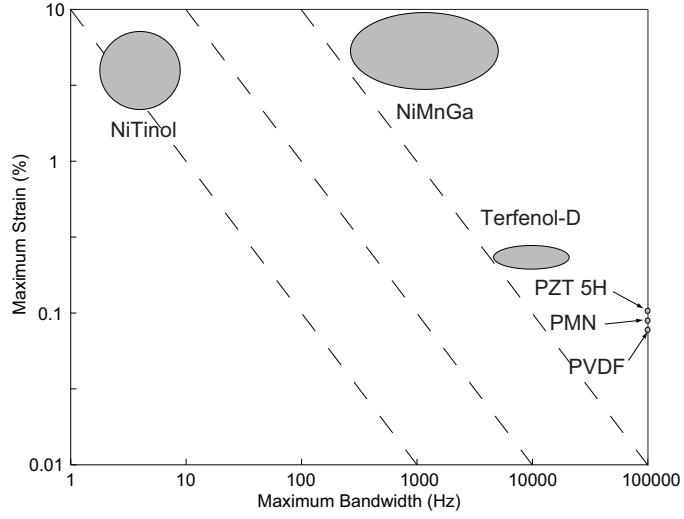


Figure 2.1: Maximum strain vs. maximum bandwidth for different smart materials.

2.1 Twin Variant Structure

When NiMnGa is cooled below a transition temperature it undergoes a diffusion-less transition from a cubic austenitic phase to a tetragonal martensitic phase. In the low temperature, martensite phase a NiMnGa sample exhibits twinning and consists of twin variants, each separated by plane boundaries. When NiMnGa is subjected to a magnetic field or mechanical stress, the proportions of the variants will change and result in shape change. Fig. 2.2 shows the evolution of variant structure with applied magnetic fields. The available macroscopic strain of NiMnGa can be calculated as $\epsilon_0 = |1 - c/a|$ by rearrangement of the variants [43].

The crystal lattice of NiMnGa martensite depends strongly on the chemical composition. Known martensite structures are the five layered tetragonal or slightly

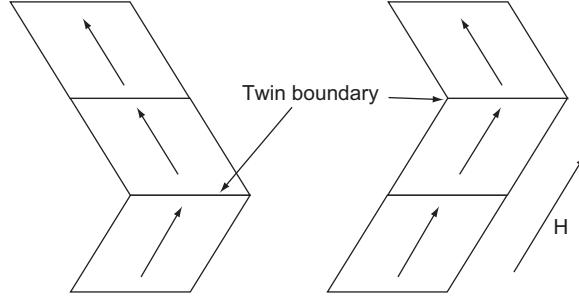


Figure 2.2: Two-dimensional representation of field-induced twin-boundary motion.

monoclinic martensite (5M), the seven layered orthorhombic or slightly monoclinic martensite (7M) and the non-modulated tetragonal martensite (T) [51]. The NiMnGa material used in this dissertation has a 5M tetragonal structure in its martensitic phase and a maximum magnetic field induced strain of 6%.

When placed in a magnetic field, the twin boundary motion is driven by the Zeeman energy difference between adjacent twin variants, which is defined as $-(\mathbf{M}_1 - \mathbf{M}_2) \cdot \mathbf{H}$, due to their nearly orthogonal magnetic easy axes and large magnetocrystalline anisotropy. The large anisotropy implies that the magnetic field energy produces reorientation of the twin variants as the moments rotate while remaining attached to the c -axis of the tetragonal crystal. In materials in which the magnetocrystalline anisotropy is weak or intermediate, the magnetization may rotate relative to the c -axis as discussed in [43].

For Ni₂MnGa, it has been found that the twin boundaries form a nearly 90° domain wall. Fig. 2.3(a) shows the twins structure of tetragonal NiMnGa obtained

from in situ optical and magneto-optical observations [35]; a schematic representation is given in Fig. 2.3(b), in which the wide strips are the twin variants with different orientations. 180° domain walls can also be seen in each variant.

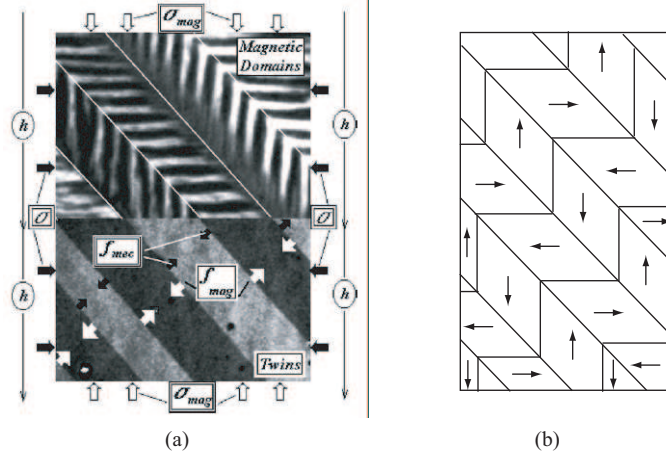


Figure 2.3: (a) Twin and microstructure of 5M martensitic phase of NiMnGa obtained from in situ optical and magneto-optical observations. (b) Schematic representation of the twin structure.

2.2 Strain Mechanism

As discussed in Chapter 1, magnetic fields are usually applied to drive the sample while perpendicular compressive stresses are used to restore the sample. The details of the strain mechanism can be found in [36, 44, 53]. A two-dimensional simplified representation of the NiMnGa sample is shown in Fig. 2.4. In panel (a), the NiMnGa consists of two martensite variants separated by twin boundaries. Each variant has an easy magnetization direction, which is parallel to the c -axis, and a hard magnetization

direction, which is parallel to the a -axis [28]. Variants with the easy magnetization direction parallel to the magnetic field are called magnetic field-preferred variants, while variants with the easy magnetization direction perpendicular to the magnetic field are called stress-preferred variants. As the transverse magnetic field intensity increases as in panel (b), the volume fraction of field-preferred variants will grow at the expense of transverse variants, which results in a growth of sample axial length, until the sample becomes a single field-preferred variant. When the magnetic field is removed, the length of the sample does not change because of the lack of a restoring force, as shown in panel (c). Since compressive stresses favor the same variants, perpendicular stress is applied to recover the sample as shown in panel (d).

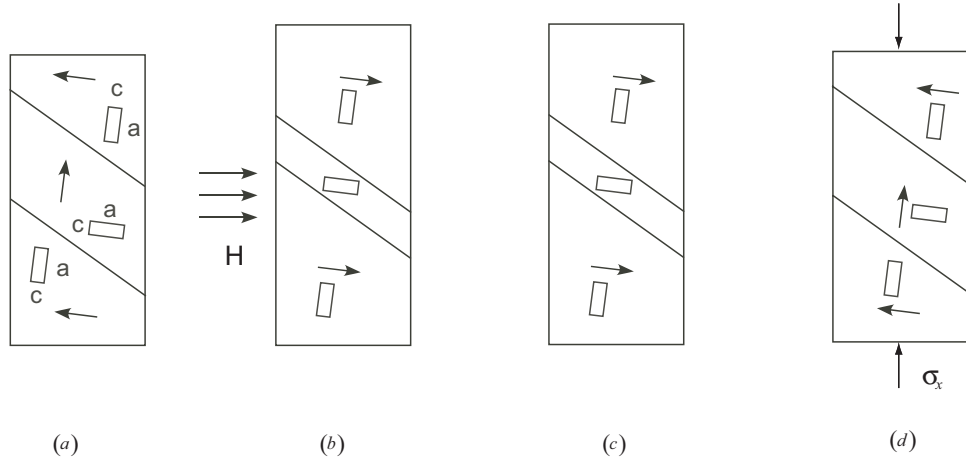


Figure 2.4: Strain mechanism with perpendicular fields and stresses: (a) initial status with zero field and stress; (b) volume fraction change when applying magnetic field; (c) removal of external field; (d) restoring the sample with orthogonal mechanical stress.

We have developed an alternative manner to induce bidirectional deformations in NiMnGa [39]. Reversible strains of -0.41% are obtained in a single crystal $\text{Ni}_{50}\text{Mn}_{28.7}\text{Ga}_{21.3}$ when exposed to alternating magnetic fields along the $[001]$ direction of the parent austenite phase without any external restoring force. This behavior is significant as it makes it possible to drive NiMnGa with a solenoid coil wrapped around the material and a magnetic circuit for providing closure of the magnetic flux. This configuration leads to higher efficiency than is possible to achieve with the conventional electromagnet drive associated with the mechanism shown in Fig. 2.8.

This behavior cannot be explained by the strain mechanism for perpendicular configurations, pointing to the existence of bias or residual stresses built in the alloy during the crystal growth. The bias stresses are attributed to high-strength pinning sites or point defects in the alloy which act as localized energy potentials that oppose twin boundary motion and provide an otherwise nonexistent restoring force when the magnetic field is removed.

The pinning sites that enable bidirectional magnetic field induced strain without the need for external restoring forces in the martensite are assumed to manifest as residual stresses oriented in the radial direction of this sample. It has been shown that NiMnGa alloys are extremely susceptible to impurities; sulfide and tantalum inclusions, and titanium-rich precipitates have been observed [46]. It was assumed that for the large, incoherent S and Ta inclusions observed, dislocations would have to loop around the impurities in order for twin boundary motion to occur. Since

the observed Ti precipitates are much smaller than the S and Ta inclusions, it was argued that the mechanism of dislocation motion in the presence of Ti precipitates is most likely cutting through the particles, as opposed to looping. By cutting, the dislocations form two new interfaces which provide a low-energy path for dislocation movement as compared to looping around the particles. It was estimated that the small Ti-rich precipitates have a strength of approximately $0.53 K_u$, thus acting as pinning sites which could be overcome by the application of sufficiently large magnetic fields. These small precipitates do not seem to impact the MFIS of the alloys studied as strains of 6% were observed.

In this context, low-energy pinning sites are assumed to not contribute to the mechanism for reversible MFIS in the alloy investigated; during the first few field cycles after manufacture of the alloy, the twin boundaries have unattached from these sites and permanently attached to higher-energy sites. Hence, the twin boundaries are normally pinned to point defects whose energy is greater than the anisotropy energy (Fig. 2.5 (a)). When a small magnetic field is applied along the $[001]$ direction, the twin boundaries attempt to displace according to the standard mechanisms for twin variant reorientation, but the Zeeman energy that drives the motion of the twin boundaries is insufficient to completely overcome the energy potential of the pinning sites. Instead, the twin boundaries loop around the impurities and as they do work against the pinning sites, energy is dissipated (Fig. 2.5 (b)(c)). Saturation is achieved when the Zeeman energy is large enough to overcome the anisotropy

energy and the magnetic moments become aligned with the field without changing the orientation of the crystal. When the field is removed, the anisotropy energy returns the magnetic moments to the easy c -axis of the crystal and the pinning site energy provides a restoring mechanism for the twin boundaries, returning the sample to its original length and magnetization value (Fig. 2.5 (d)). The pinning energy can thus be interpreted as an internal bias stress σ_x oriented perpendicular to the $[001]$ direction, as shown in Fig. 2.5. Due to the competing effect of the internal bias stress and the external magnetic field, excessive pinning energy would render the alloy inactive as the available Zeeman pressure would be insufficient to drive the motion of twin boundaries away from the pinning sites. This theory provides an explanation not only for the reversibility of the strain in the absence of an externally applied stress or field, but also reduced deformations relative to alloys capable of over 6% strain, in which twin boundary is largely unimpeded.

2.2.1 Modeling Literature Review

To quantitatively describe the magnetic field induced strain and magnetization of NiMnGa, various models have been proposed. In 1998, O’Handley [43] first proposed a simple phenomenological model for the magnetization process and field-induced strain by twin-boundary and phase-boundary motion of Ni₂MnGa for strong, weak and intermediate anisotropy cases. The Zeeman energy difference and the anisotropy energy difference between the twin variants are proposed to be the driving force for

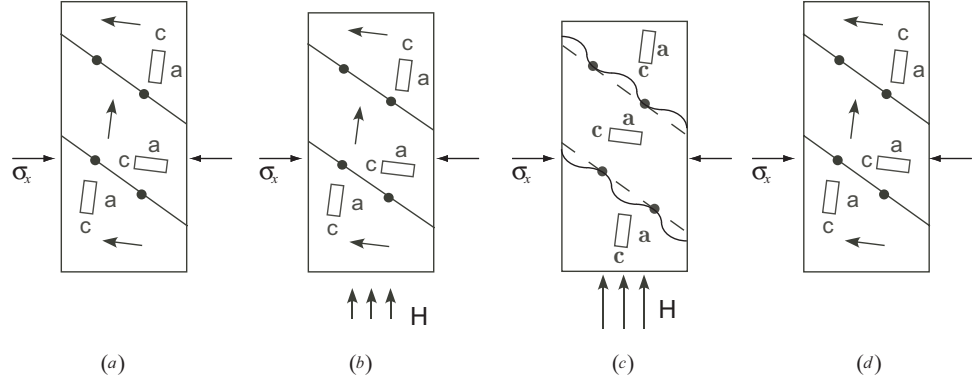


Figure 2.5: Strain mechanism with collinear fields and stresses: (a) initial status with internal bias stress; (b)(c) volume fraction change with small and large axial magnetic field; (d) removal of external field.

twin boundary motion in first two cases. The model develops a free energy expression using the Zeeman energy, elastic energy, and magnetic anisotropy, followed by the minimization of this free energy with respect to the variables of magnetization process and induced strain. The model explains the remanence and nearly linear field-dependent strain for H less than saturation in Ni_2MnGa . It also gives a description of the nonlinearities observed near saturation. However, there are unmodeled physics in that model, such as the effect of microstructure and defects on the magnetization and field induced strain.

James and Wuttig [27] applied the “constrained theory of magnetostriction” to predict strain versus field in a tetragonal martensite subject to an orthogonal biaxial magnetic field and uniaxial stress. They used the micromagnetic theory to define a constrained free energy, and the minimization of this constrained free energy leads

to expressions for the average strain and magnetization. There are two limitations of this model, one is that with the larger martensitic strains (e.g., 5 - 10% range) this model can lead to significant errors; the other is that the constraint free energy can be simplified by assuming the sample is ellipsoid, while it is somewhat difficult to use for general shapes.

Likhachev and Ullakko [34, 37] gave a thermodynamic consideration of the mechanical and magnetic properties of several ferromagnetic shape memory alloys such as Ni_2MnGa and developed a quantitative model describing the large magnetostrain. An appropriate thermodynamic potential was defined as the combination of specific Gibbs free energy and the magnetic energy at fixed temperature and pressure, from which the mechanical and magnetic properties of ferromagnetic shape memory alloys were obtained. The model also assumes the state equations are not completely independent functions and the stress and magnetization follow Maxwell's rule.

The models formulated by applying a general thermodynamic method can be found in Kiefer and Lagoudas [32], Faidley et al. [17] and Sarawate and Dapino [47], in which a specific free energy is defined based on the external independent variables as well as the microstructural internal state variables. From this free energy expression, constitutive equations can be derived by applying appropriate thermodynamic relations. The dissipative nature of the material behavior is explained by the evolution of the internal state variables.

Murray et al. [42] established a threshold type model to describe the field induced strain. A statistical approach was proposed by Glavatska et al. [24], which emphasizes the key role of microstress relaxation in the alloy response to magnetic fields.

This dissertation will present a model based on thermodynamic framework similar to [32, 17], and it will be discussed in more detail in the following chapter.

CHAPTER 3

CONSTITUTIVE MODEL

This Chapter presents the derivation of a constitutive model to quantify the behavior of NiMnGa under collinear magnetic field and mechanical stresses. A thermodynamic framework similar to that presented by Kiefer and Lagoudas [32] and Faidley et al. [17] is employed. The twin variant volume fraction is introduced as an internal state variable whose evolution can be used to account for the history dependence of the material behavior. The pinning site energy is incorporated by assuming that pinning sites create an effective bias stress σ_x oriented along the radial direction of the rod. This energy is shown to have a form similar to the hardening function employed by Kiefer and Lagoudas [32] and the mixing term from effective spring effect of the twin boundary by Faidley et al. [17]. The volume fraction evolution can be obtained from the system Gibbs free energy by applying appropriate thermodynamic relations. To address the problem of the variation of the density and the intensity of the pinning energy, a stochastic homogenization method is applied following techniques developed by Smith [48, 49, 50] which can yield an accurate model for the field induced strain in terms of external magnetic field and mechanical loading.

3.1 Formulation of Gibbs Free Energy

The strain mechanism for the case when the magnetic fields and mechanical loading are applied collinearly in the presence of internal bias stresses was discussed in Chapter 2. It was shown that the twin boundaries are impeded by energetically strong pinning sites, and the pinning energy provides a restoring force when the driving magnetic field is released. In the constitutive model developed in this chapter, a simplified two-dimensional structure is considered [43]. Only two variants are assumed to exist inside the specimen in this simplified model, and they are separated by a single twin boundary. Due to the fact that the 180° domain walls will disappear at very low fields, it is also assumed that each variant consists of a single magnetic domain. Since the pinning energy is too large to be overcome by the magnetic field energy, saturation will be achieved when the field energy overcomes the anisotropy energy, in which case the magnetization will deviate from the easy axis to align with the field without changing the orientation of the crystal.

The schematic structure represented by the simplified two-variant system is shown in Fig. 3.1. Variant V_1 is the transverse variant with a volume fraction $(1 - \xi)$, and variant V_2 is the axial variant with volume fraction ξ . The internal stress associated with the pinning sites, denoted σ_x , is represented by black dots. The Gibbs free energy G quantifies the thermodynamic state of the sample and is dependent on independent state variables such as temperature T , the stress tensor $\boldsymbol{\sigma}$, and the external

magnetic field \mathbf{H} . The influence of the crystallographic and magnetic microstructure on the macroscopic response is described by the volume fraction ξ . Other internal state variables such as the domain volume fraction and angle of rotation of the magnetization relative to the c -axis are neglected. Hence, it is assumed that the fields are large enough for 180-domain walls to disappear, and the magnetocrystalline energy is sufficiently high to force the magnetization vectors to stay attached to the c -axis when a field or stress are applied. Further, the system is assumed to stay at constant temperature.

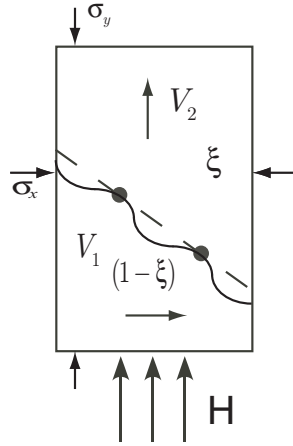


Figure 3.1: Notation and orientation of the twin-variant structure assumed for model development.

With these assumptions, the Gibbs free energy is defined as:

$$G(\boldsymbol{\sigma}, \mathbf{H}, T = \text{const}) = u - sT - E_{\text{Mechanical}} - E_{\text{Magnetic}} \quad (3.1)$$

where u is the internal energy associated with the system, s is the entropy of the system, T is the absolute temperature, $E_{Mechanical}$ is the mechanical energy, and $E_{Magnetic}$ is the energy from the external magnetic field. Using Legendre transforms, the Holmholtz energy is defined as $\psi = u - sT$. The mechanical and magnetic energy can be written as

$$E_{Mechanical} = \frac{1}{\rho} \boldsymbol{\sigma} : \mathbf{S} \boldsymbol{\sigma} \quad (3.2)$$

$$E_{Magnetic} = \frac{\mu_0}{\rho} \mathbf{M} \cdot \mathbf{H}. \quad (3.3)$$

Here, ρ is the material density, $\boldsymbol{\sigma}$ is stress, \mathbf{S} is compliance, $\mu_0 = 1.256 \times 10^{-6} \text{ N/A}^2$ is permeability of free space, \mathbf{M} is magnetization, and \mathbf{H} is magnetic field. The specific Gibbs energy for each variant can be written as

$$G(\boldsymbol{\sigma}, \mathbf{H}, T = \text{const}) = u - sT - \frac{1}{\rho} \boldsymbol{\sigma} : \mathbf{S} \boldsymbol{\sigma} - \frac{\mu_0}{\rho} \mathbf{M} \cdot \mathbf{H}. \quad (3.4)$$

On the basis of the assumed microstructure of Fig. 3.1 and the choice of variant volume fraction as the the internal state variable, the Gibbs free energy for the system can be constructed as a weighted average between the contributions of each variant. Since the interactions of these two variants are modeled as the internal stress, there is no additional mixing term as that in Refs. [32, 17]:

$$G(\boldsymbol{\sigma}, \mathbf{H}, \xi, T = \text{const}) = (1 - \xi)G^{V1} + \xi G^{V2}. \quad (3.5)$$

where G^{Vi} is the energy of the i -th variant,

$$G^{Vi}(\boldsymbol{\sigma}, \mathbf{H}, T = \text{const}) = \psi^{Vi} - \frac{1}{\rho} \boldsymbol{\sigma} : \mathbf{S}^{Vi} \boldsymbol{\sigma} - \frac{\mu_0}{\rho} \mathbf{M}^{Vi} \cdot \mathbf{H}. \quad (3.6)$$

Since the Cauchy stress and strain tensors are symmetric, $\sigma_{ij} = \sigma_{ji}$ and $\epsilon_{ij} = \epsilon_{ji}$, the indices ij can be replaced by a single index according to the following convention: Hence the external stress can be expressed by

11	22	33	23,32	31,13	12,21
1	2	3	4	5	6

Table 3.1: Index convention in tensor notation

$$\boldsymbol{\sigma} = \begin{bmatrix} \sigma_x & \sigma_y & 0 & 0 & 0 & 0 \end{bmatrix}^T.$$

The magnetic field is applied only along the axial direction, so it can be expressed as:

$$\mathbf{H} = \begin{bmatrix} 0 & H_y & 0 \end{bmatrix}^T$$

Substitution of (3.6) into (3.5) yields the final Gibbs expression for the system

$$G(\boldsymbol{\sigma}, \mathbf{H}, \xi, T = \text{const}) = \psi^{V1} - \frac{1}{\rho} S_{yy}^{V1} \sigma_y^2 - \xi \frac{\mu_0}{\rho} M_s H_y - \begin{cases} b_1 \xi + a_1 \xi^2 & \dot{\xi} > 0 \\ b_2 \xi + a_2 \xi^2 & \dot{\xi} < 0 \end{cases} \quad (3.7)$$

where $a_i = k^2 S_{11}^{V_i} / (2\rho)$ and $b_i = k S_{12}^{V_i} / \rho$, $i = 1, 2$. It should be noted that the component σ_x in the stress tensor is assumed to be a linear function of the volume fraction ξ , i.e., $\sigma_x = k\xi$. For this twin variant structure, since the only difference between the variants is their orientation, it can be assumed that their compliances are the same; in addition, the two variants are assumed to have identical Helmholtz energy, i.e., $\Delta\psi = 0$. The free energy expression can be used to obtain various thermodynamic quantities.

3.2 Evolution of the Reorientation Strain

Having obtained the Gibbs free energy for the system, the evolution of the twin variants can be derived from the second law of thermodynamics, which states that in an isolated system, a process can occur only if it increases the total entropy of the system [40]. Hence,

$$\dot{s} - \frac{r^h}{T} + \frac{1}{\rho T} \nabla \cdot \mathbf{q} - \frac{1}{\rho T^2} \mathbf{q} \cdot \nabla T \geq 0 \quad (3.8)$$

where s is entropy, T is temperature, \mathbf{q} is heat flux vector, and r^h is a distributed internal heat source.

The time derivative of the Gibbs energy given by 3.4 is

$$\frac{\partial G}{\partial t} = \dot{u} - \dot{s}T - s\dot{T} - \frac{1}{\rho} \dot{\boldsymbol{\sigma}} \cdot \boldsymbol{\epsilon}^{te} - \frac{1}{\rho} \boldsymbol{\sigma} \cdot \dot{\boldsymbol{\epsilon}}^{te} - \frac{\mu_0}{\rho} \dot{\mathbf{M}} \cdot \mathbf{H} - \frac{\mu_0}{\rho} \mathbf{M} \cdot \dot{\mathbf{H}}. \quad (3.9)$$

The first law of thermodynamics states that the increase in the internal energy of a system is equal to the amount of energy added by heating the system minus the amount lost as a result of the work done by the system on its surrounding. Mathematically, the first law can be expressed as

$$\rho \dot{u} = \boldsymbol{\sigma} \cdot \dot{\boldsymbol{\epsilon}} + \mu_0 \mathbf{H} \cdot \dot{\mathbf{M}} - \nabla \cdot \mathbf{q} + \rho r^h. \quad (3.10)$$

Substitution of \dot{u} in equation (3.10) into (3.9) and solving for \dot{s} gives

$$\dot{s} = \frac{1}{T} \left(-\frac{\partial G}{\partial t} - s\dot{T} - \frac{1}{\rho} \nabla \cdot \mathbf{q} + r^h - \frac{1}{\rho} \dot{\boldsymbol{\sigma}} \cdot \boldsymbol{\epsilon}^{te} - \frac{\mu_0}{\rho} \dot{\mathbf{H}} \cdot \mathbf{M} - \frac{1}{\rho} \boldsymbol{\sigma} \cdot \dot{\boldsymbol{\epsilon}}^r \right). \quad (3.11)$$

In this equation, the total strain is set to be the sum of the elastic strain and the magnetic field induced reorientation strain,

$$\boldsymbol{\epsilon} = \boldsymbol{\epsilon}^{te} + \boldsymbol{\epsilon}^r.$$

The time derivative of the Gibbs energy can be expanded using the chain rule [11, 12, 25, 26]

$$\frac{\partial G}{\partial t} = \frac{\partial G}{\partial T} \dot{T} + \frac{\partial G}{\partial \boldsymbol{\sigma}} \dot{\boldsymbol{\sigma}} + \frac{\partial G}{\partial \mathbf{H}} \dot{\mathbf{H}} + \frac{\partial G}{\partial \epsilon^r} \dot{\epsilon}^r + \frac{\partial G}{\partial \xi} \dot{\xi}. \quad (3.12)$$

Equations (3.11) and (3.12) can be substituted into equation (3.8) to give

$$\begin{aligned} -\rho \left(\frac{\partial G}{\partial T} + s \right) \dot{T} & - \left(\rho \frac{\partial G}{\partial \boldsymbol{\sigma}} + \boldsymbol{\epsilon}^{te} \right) \cdot \dot{\boldsymbol{\sigma}} - \left(\rho \frac{\partial G}{\partial \mathbf{H}} + \mu_0 \mathbf{M} \right) \cdot \dot{\mathbf{H}} \\ & - \left(\rho \frac{\partial G}{\partial \epsilon^r} - \boldsymbol{\sigma} \right) \cdot \dot{\boldsymbol{\epsilon}}^r - \rho \frac{\partial G}{\partial \xi} \dot{\xi} - \frac{1}{T} \mathbf{q} \cdot \nabla T \geq 0. \end{aligned} \quad (3.13)$$

The rate terms in equation (3.13) related to the external state variables such as \dot{T} , $\dot{\boldsymbol{\sigma}}$ and $\dot{\mathbf{H}}$ are independent and not constrained, so to make equation (3.13) hold, the rate terms coefficients must be zero. This yields constitutive equations for the entropy, elastic strain and magnetization,

$$\begin{aligned} s &= -\frac{\partial G}{\partial T} \\ \boldsymbol{\epsilon}^{te} &= -\rho \frac{\partial G}{\partial \boldsymbol{\sigma}} \\ \mathbf{M} &= -\frac{\rho}{\mu_0} \frac{\partial G}{\partial \mathbf{H}}. \end{aligned}$$

Due to the isothermal assumption, the temperature gradient is zero, thus equation (3.13) can be reduced to

$$-\left(\rho \frac{\partial G}{\partial \epsilon^r} - \boldsymbol{\sigma} \right) \cdot \dot{\boldsymbol{\epsilon}}^r - \rho \frac{\partial G}{\partial \xi} \dot{\xi} \geq 0 \quad (3.14)$$

Inspection of Fig. 3.1 reveals the reorientation strain rate is proportional to the rate of change of the martensitic volume fraction,

$$\dot{\epsilon}^r = \Lambda^r \dot{\xi}, \quad (3.15)$$

where Λ^r is defined as $\epsilon_s \cdot [-1 \ 1 \ 0 \ 0 \ 0 \ 0]^T$ and physically can be interpreted as a constant conversion vector to transform the volume fraction change to the reorientation strain. Since the external applied stress and magnetic field are along the y-axis only, equation (3.14) can be rewritten as [31, 32, 16]:

$$(\sigma_y \epsilon_s - \rho \frac{\partial G}{\partial \xi}) \dot{\xi} \geq 0 \quad (3.16)$$

As done in [31]

$$\pi^\xi = \sigma_y \epsilon_s - \rho \frac{\partial G}{\partial \xi} \quad (3.17)$$

is defined as the condition for the onset of twin variant motion. This thermodynamic driving force equals $\pm Y^\xi$ for the growth of the axial variant and the shrinking of the axial variant respectively, which can be obtained by fitting the experimental data.

Differentiation of equation (3.7) and substitution into equation (3.17) gives the equation of force balance

$$\pm Y^\xi = \epsilon_s \sigma_y + \mu_0 M_s H_y + \rho \begin{cases} b_1 + 2a_1 \dot{\xi} & \dot{\xi} > 0 \\ b_2 + 2a_2 \dot{\xi} & \dot{\xi} < 0 \end{cases}. \quad (3.18)$$

Equation (3.18) can be solved for the volume fraction

$$\xi = \begin{cases} \frac{1}{2\rho a_1} (-\epsilon_s \sigma_y - \mu_0 M_s H_y - \rho b_1 + Y^\xi) & \dot{\xi} > 0 \\ \frac{1}{2\rho a_2} (-\epsilon_s \sigma_y - \mu_0 M_s H_y - \rho b_2 - Y^\xi) & \dot{\xi} < 0 \end{cases}, \quad (3.19)$$

which is related to the strain by

$$\epsilon = \xi \epsilon_{th}, \quad (3.20)$$

with ϵ_{th} the maximum theoretical strain which would occur if a single boundary swept through the entire material (6%), thus producing a change in ξ from 0 to 1. For the case in which the twin boundaries are restrained by pinning sites, ξ will be limited to a much smaller range.

3.3 Stochastic Homogenization Method

Equation (3.19) provides a model for the field induced strain generated by single crystal NiMnGa when exposed to collinear magnetic fields and external stresses. The accuracy of this model is limited due to the following factors:

(i) It was assumed that the microstructure consists of only two variants and only one mobile twin boundary spanning the cross section of the sample. In reality, NiMnGa has many twin variants though only two distinct orientations. This implies that a sample will have numerous twin boundaries and thus numerous pinning sites.

(ii) The pinning sites and effective bias stress are assumed to be homogeneously distributed throughout the material and every pinning site is assumed to have the same energy. As discussed by Marioni et al. [41], in a physical material the pinning energies vary over a large range which translates into a variation of σ_x .

(iii) The magnetic field is assumed to be uniform throughout the sample. However, due to short-range interactions the magnetic field in NiMnGa can be considered to

behave locally in a fashion similar to the Weiss mean field [28]. Thus, the magnitude of the field at a given point in the material is not equal to the applied field but rather, is given by an effective field which is dependent on the applied field and the magnetization, $H_e = H + H_i = H + \alpha M$. The mean field constant α varies from point to point in the material due to differences in the lattice structure.

The above limitations are addressed by considering stochastic homogenization as proposed by Smith [48]. This approach has been proven effective in the modeling of hysteresis and constitutive nonlinearities in ferroelectric compounds, ferromagnetic materials, and shape memory alloys. For implementation, the bias stress and the interaction field are treated as statistical distributions, which results in a macroscopic model for the volume fraction of the form

$$[\xi(H, \sigma)](t) = \int_0^\infty \int_{-\infty}^\infty \nu_1(H_i) \nu_2(a_2) [\bar{\xi}(H + H_i, \sigma, a_2)](t) dH_i da_2 \quad (3.21)$$

where ν_1 and ν_2 respectively denote the probability distribution functions for (H_i) and (a_2) , and $\bar{\xi}$ is given by (3.19). Since the interaction field can be both positive and negative, a normal distribution centered at will be an appropriate choice

$$\nu_1(H_i) = c_1 e^{-H_i^2/(2b^2)}. \quad (3.22)$$

Since a_2 has to be non-negative, a lognormal distribution is considered

$$\nu_2(a_2) = c_2 e^{-(\ln(a_2/\bar{a}_2)/2c)^2}. \quad (3.23)$$

CHAPTER 4

TRANSDUCER MODEL

4.1 Solenoid Based Transducer

This chapter is focused on the modeling of magnetic field induced strain produced by NiMnGa driven in a dynamic transducer. The model development assumes that the material is driven by a longitudinal magnetic field and subjected to stresses along the same direction. The mechanism that enables bidirectional deformations under these conditions was discussed in Section 2.2. The experimental characterization is conducted on the custom made transducer shown in Fig. 4.1 [38]. The external force is applied through the pushrod; the housing, pushrod and NiMnGa sample form a closed circuit for the magnetic field. This device generally exhibits better energy efficiency and reduced mass relative to electromagnet based transducers. Further details on the construction and characterization of the transducer can be found in [38].

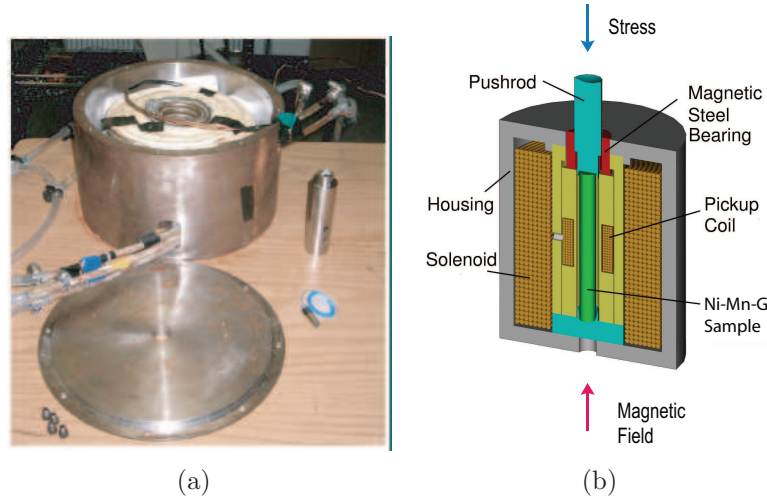


Figure 4.1: (a) Solenoid based transducer; (b) schematic representation.

4.2 Strong and Weak Form

Strong form is usually a system of ordinary or partial differential equations in space and time, together with a set of boundary and initial conditions, to describe the behavior of a physical system; weak form relaxes certain conditions in the strong form such that instead of finding an exact solution everywhere, its purpose is to find a solution satisfying the strong form on average over the domain. This section will show the derivation of the strong form of the model to describe the behavior of the NiMnGa transducer; multiplication by a test function in the H_L^1 space followed by integration will yield the weak, or variational form of the transducer model.

4.2.1 Strong Form

Fig. 4.2 shows a one-dimensional representation of the solenoid-based NiMnGa transducer. The NiMnGa rod is assumed to be homogeneous with length l , cross-section area A and longitudinal coordinate x . The density, Young's modulus and Kelvin-Voigt damping coefficient are respectively denoted by ρ , E and c . The end at $x = 0$ is fixed and the other end is connected to a mass m_l , a spring with stiffness k_l and a damper with coefficient c_l .

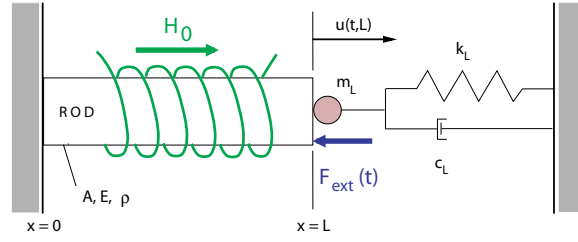


Figure 4.2: 1-dimensional representation of NiMnGa transducer.

To quantify the dynamics of the NiMnGa rod, it is reasonable to consider an infinitesimal element $[x, x + \Delta x]$ as depicted in Fig. 4.3. The total strain at location x has three components, the magnetic field induced strain, the strain from the stress at that point, and the strain associated with Kelvin-Voigt damping force, in mathematic form,

$$\frac{\partial u}{\partial x} = \epsilon + \frac{\sigma}{E} - \frac{1}{E} \left(c \frac{\partial^2 u}{\partial x \partial t} \right)$$

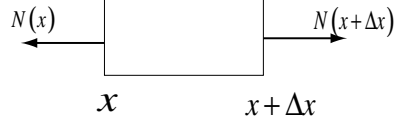


Figure 4.3: Infinitesimal element considered for force analysis.

where ϵ is the magnetic field induced strain described by equation (3.19). Reorganizing this equation gives the stress at a point $\sigma(x, t)$ in the form of

$$\sigma(t, x) = E \frac{\partial u}{\partial x}(t, x) + c \frac{\partial^2 u}{\partial x \partial t}(t, x) - E \epsilon(t, x). \quad (4.1)$$

The uniaxial resultant force can be obtained by integrating the uniaxial stress across the rod, which is given by:

$$N(t, x) = \int_A \sigma dA = \sigma(t, x)A = EA \frac{\partial u}{\partial x}(t, x) + cA \frac{\partial^2 u}{\partial x \partial t}(t, x) - EA \epsilon(t, x). \quad (4.2)$$

According to Newton's second law of motion, the balance of forces for the element can be expressed as

$$N(t, x + \Delta x) - N(t, x) = \int_x^{x+\Delta x} \rho A \frac{\partial^2 u}{\partial t^2}(t, x) dx, \quad (4.3)$$

taking the derivative of equation (4.3) with respect to x yields

$$\frac{\partial N}{\partial x}(t, x) = \rho A \frac{\partial^2 u}{\partial t^2}(t, x). \quad (4.4)$$

This is the strong form of the model for the internal rod dynamics.

To make the model complete, appropriate boundary conditions and initial conditions have to be specified. It is first noted that one end of the rod is fixed in the

transducer, which satisfies the condition $u(t, 0) = 0$ at $x = 0$. At the end $x = L$, force balance yields the second boundary condition

$$N(t, L) = -k_l u(t, L) - c_l \frac{\partial u}{\partial x}(t, L) - m_l \frac{\partial^2 u}{\partial x^2}(t, L).$$

To summarize, the boundary conditions have the form

$$\begin{cases} u(t, 0) = 0 \\ N(t, L) = -k_l u(t, L) - c_l \frac{\partial u}{\partial x}(t, L) - m_l \frac{\partial^2 u}{\partial x^2}(t, L) \end{cases} \quad (4.5)$$

Zero initial deformation and velocity give the initial conditions as

$$\begin{cases} u(0, x) = 0 \\ \frac{\partial u}{\partial x}(0, x) = 0 \end{cases} \quad (4.6)$$

The combination of equations (4.4)-(4.6) yields the strong form of the model. To solve for the deformation of the transducer, two essential steps are taken to that end:

- (i) Rephrase the original system partial differential equation in its weak, or variational form.
- (ii) Discretize the weak form in a finite dimensional space.

These two steps result in a large but finite dimensional linear problem whose solution will approximately solve the original boundary value problem. This finite dimensional problem is then implemented in Matlab. From the strong form several weak forms can be obtained by selectively weakening strong connections, which can be developed either via integration by parts or Hamiltonian energy principles. In weak form, displacements and tests functions are differentiated only once compared with the second derivatives required in the strong form. This reduces the smoothness requirements on the finite element basis when constructing an approximation method.

4.2.2 Weak Form

To construct a weak form of the model, the state u in the state space $X = L^2(0, L)$ is considered, and the space of test functions is taken to be $V = H_L^1(0, L) \equiv \{\phi \in H^1(0, L) \mid \phi(0) = 0\}$ [14]. Multiplication by test functions followed by integration over the length of the rod yields the weak form of the model. For all $\phi \in V$, there exist

$$\begin{aligned} \int_0^L \rho A \frac{\partial^2 u}{\partial t^2} \phi \, dx &= - \int_0^L \left[EA \frac{\partial u}{\partial x}(t, x) + cA \frac{\partial^2 u}{\partial x \partial t} - EA \epsilon(t, x) \right] \frac{\partial \phi}{\partial x} \, dx \\ &\quad - \left[k_l u(t, L) + c_l \frac{\partial u}{\partial t}(t, L) + m_l \frac{\partial^2 u}{\partial t^2} \right]. \end{aligned} \quad (4.7)$$

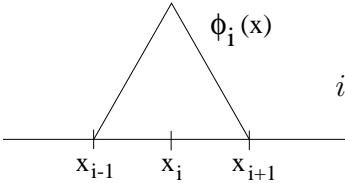
4.3 Numerical Approximation

Having obtained the weak form of the system, the next step is to solve for the solution to equation (4.7), to that end, either the Rayleigh-Ritz approximation method or Galerkin's approximation method can be used. Since the Galerkin method has all the advantages of the Ritz method but can be used in a more general case, for example when there is no functional for the problem [7, 10, 15], it will be taken to discretize in space and the trapezoidal method will be taken to discretize in time.

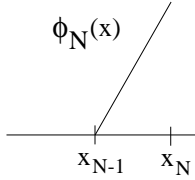
4.3.1 Galerkin Discretization

In the area of numerical analysis, Galerkin discretization is a general method to solve differential equations by converting them from a continuous problem to a discrete one. It applies the method of variation to a function space and then applies

some constraints on the function space to characterize the space with a finite set of basis functions. As briefly discussed in 4.2.2, the test function space V is a subspace of the L^2 -norm space X , but as is customary, they are assumed to have the same bases. For $u \in X$, it can be expressed by $u = \sum_0^n c_n \phi_n$. In implementation, the interval $[0, L]$ of the sample is partitioned in N subintervals of stepsize $h = L/N$. The spatial basis is comprised of linear splines or “hat functions” [45], defined at points $x_i = i h$ ($i = 0, 1, \dots, N$) as follows

$$\phi_i(x) = \frac{1}{h} \begin{cases} (x - x_{i-1}), & x_{i-1} \leq x < x_i \\ (x_{i+1} - x), & x_i \leq x < x_{i+1} \\ 0, & \text{otherwise} \end{cases}$$


$i = 1, \dots, N - 1$

$$\phi_i(x) = \frac{1}{h} \begin{cases} (x - x_{N-1}), & x_{N-1} \leq x \leq x_N \\ 0, & \text{otherwise.} \end{cases}$$


The displacements $u(t, x)$ are approximated using the expansion

$$u^N(t, x) = \sum_{j=1}^N u_j(t) \phi_j(x), \quad (4.8)$$

defined in the subspace $H^N = \text{span}\{\phi_j\}_{j=1}^N$, which through the construction of the basis functions satisfies the respective boundary conditions in the transducer.

The approximate solution (4.8) is substituted into (4.7), along with test functions ϕ equal to the basis functions, to form a second-order temporal vector system

$$M \ddot{\vec{u}}(t) + C \dot{\vec{u}}(t) + K \vec{u}(t) = \vec{F}[\epsilon(t)], \quad (4.9)$$

where $\vec{u}(t) = [u_1(t), \dots, u_N(t)]^T$.

The mass, damping and stiffness matrices have the form

$$\begin{aligned}
[M]_{ij} &= \begin{cases} \int_0^L \rho A \phi_i \phi_j dx & , \quad i \neq n \quad \text{and} \quad j \neq n \\ \int_0^L \rho A \phi_i \phi_j dx + m_L & , \quad i = n \quad \text{and} \quad j = n \end{cases} \\
[C]_{ij} &= \begin{cases} \int_0^L c_D A \phi'_i \phi'_j dx & , \quad i \neq n \quad \text{and} \quad j \neq n \\ \int_0^L c_D A \phi'_i \phi'_j dx + C_L & , \quad i = n \quad \text{and} \quad j = n \end{cases} \\
[K]_{ij} &= \begin{cases} \int_0^L E A \phi'_i \phi'_j dx & , \quad i \neq n \quad \text{and} \quad j \neq n \\ \int_0^L E A \phi'_i \phi'_j dx + K_L & , \quad i = n \quad \text{and} \quad j = n \end{cases}
\end{aligned}$$

while the excitation vector is defined by

$$\vec{F}_i[\epsilon(t)] = \int_0^L E A \epsilon(t, x) \phi'_i(x) dx.$$

The second-order system (4.9) can be expressed as a first-order system of the form

$$\begin{aligned}
\dot{\vec{y}}(t) &= P \vec{y}(t) + \vec{B}(t) \\
\vec{y}(0) &= \vec{y}_0,
\end{aligned} \tag{4.10}$$

where $\vec{y}(t) = [\vec{u}(t), \dot{\vec{u}}(t)]^T$ is the generalized solution, and

$$P = \begin{bmatrix} 0 & I \\ -M^{-1}K & -M^{-1}C \end{bmatrix}, \quad \vec{B}(t) = \begin{bmatrix} 0 \\ -M^{-1}\vec{F}(t) \end{bmatrix}.$$

4.3.2 Trapezoidal Method

The first-order system (4.10) must be discretized in time for numerical implementation. To this end, a standard trapezoidal discretization with step size Δt is considered:

$$\begin{aligned}
\vec{y}_{j+1} &= \mathcal{P} \vec{y}_j + \frac{1}{2} \mathcal{B} \left[\vec{B}(t_j) + \vec{B}(t_{j+1}) \right] \\
\vec{y}_0 &= \vec{y}(0),
\end{aligned}$$

where $t_j = j\Delta t$ and \vec{y}_j approximates $\vec{y}(t_j)$. The matrices

$$\mathcal{P} = \left[I - \frac{\Delta t}{2} P \right]^{-1}, \quad \mathcal{B} = \Delta t \left[I - \frac{\Delta t}{2} P \right]^{-1}$$

need to be created only once when numerically or experimentally implementing the method.

4.4 Experiments and Results

The experiments in which the strain vs. applied magnetic field response for $\text{Ni}_{50}\text{Mn}_{28.7}\text{Ga}_{21.3}$ is measured were reported by Malla et al. [39], from which, data is used to validate the model developed in previous sections. The experiments were run on a cylindrical rod of $\text{Ni}_{50}\text{Mn}_{28.7}\text{Ga}_{21.3}$ with the dimensions of $0.25 \text{ in}^2 \times 0.9 \text{ in}$. The NiMnGa sample is actuated in a sinusoidal field of amplitude 700 kA/m and frequency 0.1 Hz. A water-cooled solenoid transducer as Fig4.1(a) is employed. It is shown in [39] that the magnetic field varies along the length of the solenoid; to minimize the error caused by this inhomogeneity, the sample is placed in the center of the transducer. A pick-up coil is used to monitor the magnetic flux density. The field induced strain is measured with a linear variable differential transformer (LVDT), which is mounted to the pushrod in the NiMnGa transducer. Three thermocouples, which are placed at the inlet, outlet of the cooling coils and the inner surface of the solenoid respectively, are used to monitor the system temperature to ensure that all testing is done in the same temperature range and the ambient temperature variation

is effectively controlled within $\pm 1^\circ F$. Further details of the experiments can be found in [39].

4.4.1 Parameter Identification

Chapter 3 stated that the final constitutive material model is obtained by stochastic homogenization of a hysteresis kernel model. To that end, parameters in the constitutive kernel (3.19) need to be determined from the experimental data, some of which can be measured directly from experiments. For example, the saturation magnetization M_s can be measured using a pick-up coil and it is identified with the value of 385kA/m [38]; Malla also measured the maximum reversible strain ϵ_s of $\text{Ni}_{50}\text{Mn}_{28.7}\text{Ga}_{21.3}$ sample under various loading conditions [38]. The force density necessary to provided the onset of variant reorientation (Y^ξ) is measured as 209570 Nm/m³ by Kiefer [31].

Other parameters such as a_1 , a_2 , b_1 , and b_2 can be determined phenomenologically by fitting the desired shape of the hysteresis loop to data for a particular applied stress. Three points indicated in Fig. 4.4 provide the following information

- (1) magnetic field at which the sample has a zero strain;
- (2) residue strain at zero field; and
- (3) magnetic field at which the sample starts the recovery.

With these measurements, the equations in Table 4.1 [17, 39] can be used to calculate the parameters needed to implement model (3.19).

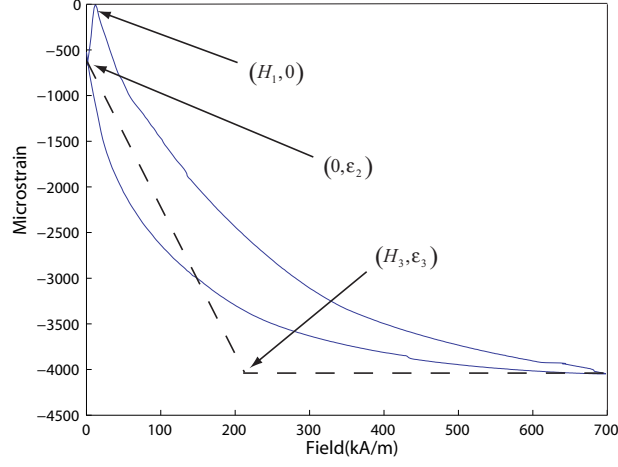


Figure 4.4: Data points for parameters identification.

ϵ	$=$	$\xi \epsilon_{th}$
a_1	$=$	$1.5a_2$
a_2	$=$	$\frac{\mu_0 M_s H_3 \epsilon_{th}}{2(\epsilon_s - \epsilon_2)}$
b_1	$=$	$\epsilon_s \sigma_y + \mu_0 M_s H_1 - Y^\xi$
b_2	$=$	$\epsilon_s \sigma_y + Y^\xi - 2a_2 \frac{\epsilon_2}{\epsilon_{th}}$

Table 4.1: Model parameters identified from experimental data.

Parameters for the external system include the loading mass m_l , which can be measured directly, external spring stiffness k_l , and damping coefficient c_l ; for the NiMnGa rod, parameters to be determined are the density ρ , elastic modulus of the rod E and the Kevin-Voigt damping coefficient c . To simulate the actual experimental conditions, the spring stiffness k_l in the external system is set to zero in the

model, while the damping coefficient c_l associated with the friction between the transducer push rod and bearing is obtained through fitting to experimental data. The elastic modulus and the Kevin-Voigt damping coefficient are found from dynamic measurements in Ref. [18].

4.4.2 Stochastic Homogenization Implementation

Section 3.3 pointed out the limitations of the hysteresis kernel model with the assumptions of uniform pinning energy density and intensity as well as uniform internal magnetic field. To address the problem caused by this, a normal distribution function is assigned to the interaction field centered at 0 since the Weiss interaction field is known to have both positive and negative values; from the definition of the pinning energy related parameter a_2 , it can be seen that the values for a_2 will never be negative; to satisfy this condition, its distribution is chosen to be lognormal. The shapes of these distributions can be found in Fig. 4.5. To illustrate the effect of the distribution on the slopes of the hysteresis kernels, several constitutive kernels are shown in Fig. 4.6.

For the implementation of the homogenized model

$$[\xi(H, \sigma)](t) = \int_0^\infty \int_{-\infty}^\infty \nu_1(H_i) \nu_2(a_2) [\bar{\xi}(H + H_i, \sigma, a_2)](t) dH_i da_2, \quad (4.11)$$

Gaussian quadrature rule is considered to approximate the integrals[8, 52]. A quadrature rule is an approximation of the definite integral of a function, usually stated as a weighted sum of function values at specified points within the domain of integration.

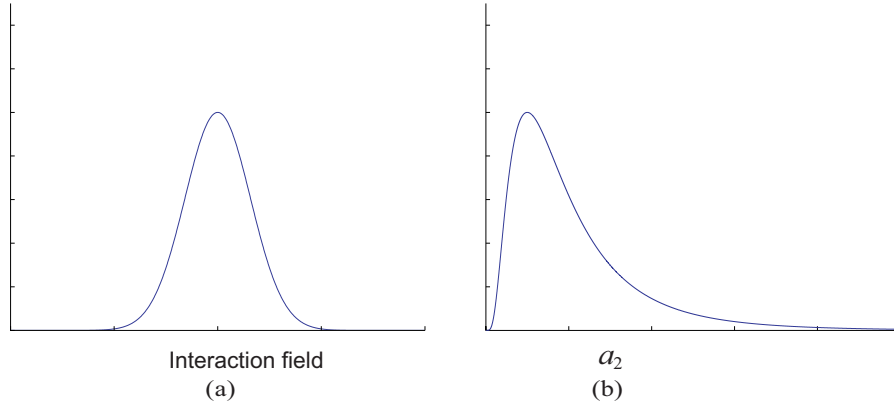


Figure 4.5: (a) Interaction field distribution. (b) Slope parameter distribution.

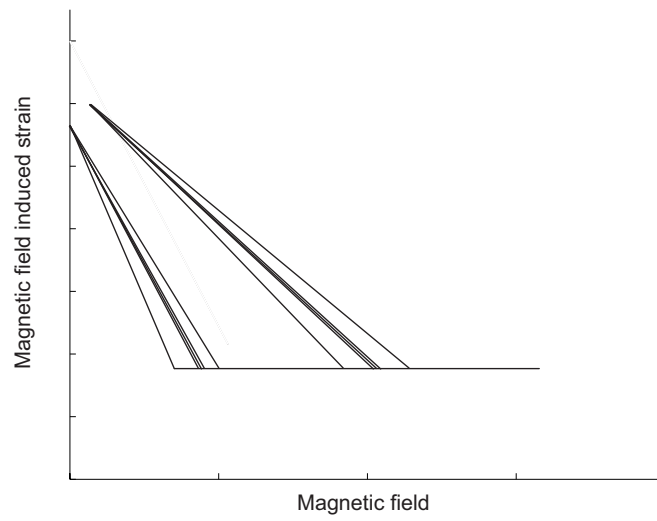


Figure 4.6: Kernels with different slopes.

The power of this numerical integration method is that through the use of several evaluation points and appropriate weights, the approximation can be made with very few calculations with good accuracy. An n -point Gaussian quadrature rule can be expressed in the form of

$$\int_{-1}^1 f(x) dx \approx \sum_{i=1}^n w_i f(x_i) \quad (4.12)$$

where x_i are the suitable points chosen in the domain of integration, and w_i are the weights assigned for each point. It is worth noting that the integral domain in equation (4.14) is from -1 to 1, which requires that an integral over $[a, b]$ must be modified for applying the standard Gaussian quadrature rule, which can be done by the transformation

$$\int_a^b f(x) dx = \frac{b-a}{2} \int_{-1}^1 f\left(\frac{b-a}{2}x + \frac{a+b}{2}\right) dx. \quad (4.13)$$

Consequently, the approximation of an integration over $[a, b]$ with the application of n -point Gaussian quadrature rule can be rewritten as

$$\int_a^b f(x) dx \approx \sum_{i=1}^n w_i f\left(\frac{b-a}{2}x_i + \frac{a+b}{2}\right) \quad (4.14)$$

For simplicity, the 4-point Gauss quadrature rule is used in this dissertation, in which four appropriate evaluation points and weights are given in Table 4.2

Another modification to the standard Gaussian quadrature method is made in the implementation of the model in this dissertation. To increase the accuracy of the approximation, the whole integration domain is divided into n subdomains; with the application of Gaussian quadrature rule to each subdomain, the expression for the

x_i	w_i
-0.861136311594053	0.347854845137454
-0.339981043584856	0.652145154862546
0.339981043584856	0.652145154862546
0.861136311594053	0.347854845137454

Table 4.2: 4-point Gaussian quadrature points and weights

approximation of the problem becomes

$$\begin{aligned}
[\xi(H, \sigma)](t) &= \int_0^\infty \int_{-\infty}^\infty \nu_1(H_i) \nu_2(a_2) [\bar{\xi}(H + H_i, \sigma, a_2)](t) dH_i da_2 \\
&= \int_{a_{2,min}}^{a_{2,max}} \int_{-H_{i,max}}^{H_{i,max}} \nu_1(H_i) \nu_2(a_2) [\bar{\xi}(H + H_i, \sigma, a_2)](t) dH_i da_2 \\
&= \sum_{i=1}^{n \times 4} \sum_{i=1}^{n \times 4} W_1(H_i) W_2(a_2) [\bar{\xi}(H + H_i, \sigma, a_2)](t). \tag{4.15}
\end{aligned}$$

The equation (4.15) shows that an extension to a double integral is used to incorporate both variables, and a composite approach is taken to divide the overall interval into smaller intervals in which the 4-point quadrature is applied. By making use of the matrix operations, this approximation can be easily implemented in Matlab; the coding for the model can be found in the Appendix.

The constrained optimization toolbox in Matlab is used to identify the distribution function parameters n, b, c , and \bar{a}_2 in equations (3.22) and (3.23). The constrained optimization routine minimizes the mean square error between the model and measured data under each loading condition. The parameters for each of the four loading cases are listed in Table 4.3, it is shown in [16] that simulation with these parameters closely predicts the data in each case, while applying the parameters obtained from

σ	$-0.0125MPa$	$-0.13MPa$	$-0.27MPa$	$-0.41MPa$	<i>Optimized</i>
n	1.165	1.1417	1.0894	1.0287	1.1207
b	1030000	700910	871820	1336300	753250
c	0.80761	1	1	0.99856	0.99901
\bar{a}_2	100	121.66	100	100	103.04

Table 4.3: Model parameter values.

one loading case to another yields unnegligible error. To address this problem, rather than applying the individual optimization, the parameters are obtained by minimizing the overall mean square error for all four loading cases, which are listed in the last column in Table 4.3. The details of the error analysis can be found in [16].

4.4.3 Model Results

Table 4.4 summarizes the material properties and constitutive kernel parameters. Together with the set of parameters optimized to minimize the total error across all four loading cases in Table 4.3, the comparison between the transducer model and the experimental data is provided in Fig 4.7, in which the red curves are from the model and the blue dash-line curves represent the experimental data. This figure shows that by incorporating the structure dynamics of the NiMnGa transducer, the model can match closely the experimental data, which shows a promising future of this model in the design and control of this type of actuator in real applications.

Permeability of free space	$\mu_0 = 1.256 \times 10^{-6} N/A^2$
Saturation magnetization	$M_s = 622 kA/m$
Theoretical maximum strain	$\epsilon_{th} = -0.06$
Difference in compliance for two variants	$\Delta S_{yy} = 0$
NiMnGa density	$\rho = 7659 kg/m^3$
Onset of variant reorientation	$Y^x = 209570 Nm/m^3$
Saturation strain	$\epsilon_s(\sigma) = \text{dependent on external loading}$
Magnetic field at zero strain	$H_1 = 10750$
Residue strain	$\epsilon(\sigma) = \text{dependent on external loading}$

Table 4.4: Model parameter values.

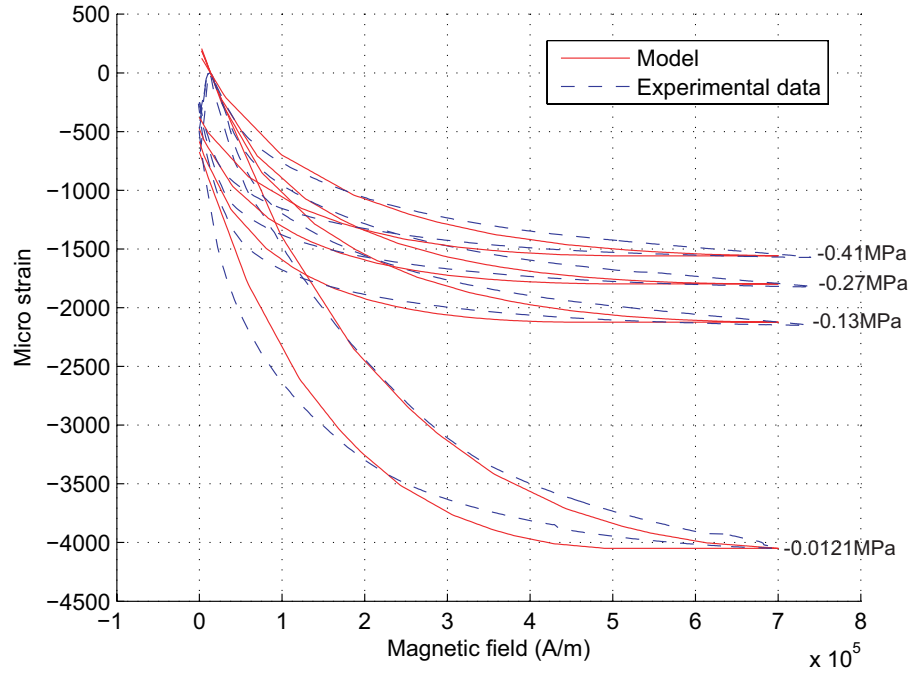


Figure 4.7: Comparison of model results and experimental data for various loads.

CHAPTER 5

POWER LOSSES AND MAGNETIC FIELD DIFFUSION

5.1 Background

The previous chapter discussed the dynamics of the NiMnGa transducer and computation methodology for implementation. However, although actuator devices are subjected to AC excitations, most measurements of magnetic response of the active material element in the literature are performed under DC or quasi-DC conditions. This is partly due to the unsurmountable difficulty in measuring the magnetic field decay inside a sample as the frequency is increased. The differences between DC and AC responses in a magnetic material depend on a number of factors, including the electrical conductivity and permeability, the rate at which magnetic moments can rotate into the field direction, and the frequency of the applied field. To address this question, a qualitative analysis of the influence of these factors is provided in this chapter to establish the mechanism of energy dissipation in the material.

5.1.1 Eddy Currents

In electromagnetic theory, Maxwell-Farady equation

$$\nabla \times \mathbf{E} = -\frac{\partial \mathbf{B}}{\partial t} \quad (5.1)$$

states that the induced electric field in a close loop of wire is directly proportional to the rate of change of the magnetic induction through the loop. In equation (5.1), \mathbf{B} is the magnetic induction and \mathbf{E} is the electric field. If a NiMnGa sample is placed inside an AC magnetic field, electrical current will be induced in the form of eddies due to the electric conductivity of NiMnGa sample, and hence the energy will be wasted as heat. In addition, equation (5.1) shows that the induced current will always try to produce the magnetic flux which opposes the flux produced by surrounding magnetic field, in high frequencies, the loss of the magnetic field could be so tremendous that the actuator would fail to work because of the loss of the driving magnetic field energy.

In real applications, to get rid of eddy currents, slits can be cut in conductive materials so that large eddy current cannot occur. It can be widely found that the metal cores in transformers are often assembled in small laminations with an insulator in between. This prevents AC energy from being lost to eddy currents generated within the magnetic core.

In addition to the frequency dependent power losses created by eddy current, some other formats of losses resulting from the microstructure of the material will be introduced in next section. In conjunction with the DC hysteresis model presented in previous chapter, the frequency dependent loss components will provide a description of the field induced strain in dynamic situations.

5.1.2 Eddy Current Power Loss Literature Review

Trying to interpret the eddy current losses physically, Bertotti [1, 2, 4, 5] proposed that the basic physical mechanism responsible for the general behavior of eddy current losses versus frequency is the competition between the external field, which is assumed to be applied uniformly in the sample, and highly inhomogeneous local counter-fields, due to magnetostatic and coercive effects. The concept of magnetic object, corresponding to a group of neighboring walls evolving in a highly correlated fashion, is introduced in order to take into proper account the role of short-range internal correlation fields. He assumes a random spatial distribution of the magnetic objects, and the dynamic loss is a function of the number of magnetic objects which are simultaneously active. In the literature, the total power losses in the ferromagnetic materials are put into three categories:

- (1) the hysteresis related power loss;
- (2) classical power loss;
- (3) and anomalous power loss. So the total loss can be written in the form of

$$P^{loss} = P^{hyst} + P^{classical} + \frac{bP^{hyst}}{2} \left(\sqrt{1 + 2af_m} - 1 \right), \quad (5.2)$$

where the hysteresis power loss and classical loss in materials of fine domain structure are functions of microscopic magnetization dynamics. In the third term of the equation, f_m represents the magnetizing frequency, while a and b are parameters related to the local correlation properties of the domain wall jumps.

In implementation, a general statistical theory of losses is applied, the total loss is calculated by a superposition of many eddy current patterns generated by different jumps corresponding to different physical conditions of domain structure, magnetizing frequency, etc. However, although the classical power loss is brought up in [4, 5], its definition is not explicitly provided.

Following the framework of Bertotti, Jiles [29, 30] extended the quasi-static hysteresis equation to account for energy losses resulting from the generation of eddy currents in electrically conducting materials. He posited that the power loss due to eddy currents consists of two terms, one of which depends on the square of rate of change of the induction, i.e., $(dB/dt)^2$, while the other term, which is the anomalous power loss defined in Bertotti[4, 5], is redefined to be dependent on $(dB/dt)^{1.5}$. These two terms are incorporated into a time dependent hysteresis model so that the quasi-static hysteresis curves are shown to be a limiting case of the more general frequency dependent model. This dissertation will take the same method on ferromagnetic shape memory alloy NiMnGa to make the quasi-static model developed in Chapter 2 adapted to high frequency applications.

5.2 Hysteresis Model With Eddy Current Loss

This section will present a hysteresis model with the eddy current loss for ferromagnetic shape memory alloy NiMnGa. In Jiles[30], the power losses in an electrically

conductive material can be decomposed into the sum of a hysteresis and a dynamic contribution, in mathematic form:

$$\begin{aligned} P^{loss} &= P^{hyst} + P^{dyn} \\ &= P^{hyst} + P^{EC} + P^A, \end{aligned} \tag{5.3}$$

where P^{hyst} is the hysteresis loss contribution, which can be directly calculated from the constitutive model. P^{EC} and P^A are classical eddy current loss and anomalous (or excess) loss respectively. In this model, the skin effect is ignored, in other words, the magnetic field is assumed to uniformly penetrate through the sample and the losses are only dependent on the frequency of driving field. For a solid active material, this assumption is limiting due to the skin depth effect on the magnetic field inside the material, so it is accurate when the transducer components are laminated.

Now it is the time to show the definition of dynamic power losses. The classical eddy current instantaneous power loss per unit is obtained by solving the Maxwell equation $\nabla \times \mathbf{E} = -d\mathbf{B}/dt$ for a given geometry, and it is found to be proportional to the square of the rate of change of magnetization, the details can be found in Chikazumi [9],

$$P_{EC} = \frac{\mu_0^2 d^2}{2\rho\beta} \left(\frac{dM}{dt} \right)^2. \tag{5.4}$$

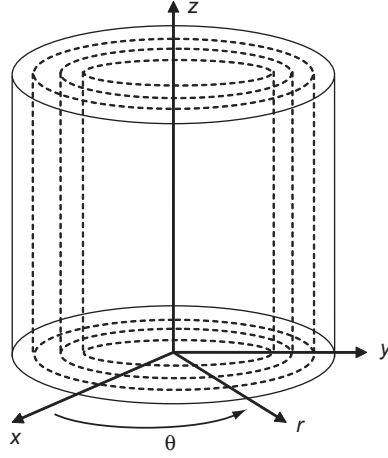


Figure 5.1: Laminated cylindrical sample.

In equation (5.4) ρ is the resistivity (Ωm), d is the diameter of the NiMnGa rod (m), and β is a geometrical factor which takes the value of 16 for cylinders.

As mentioned, the anomalous power loss results from changes in the domain configuration [6, 30]. Instead of applying the statistical method by Bertotti, this component of the power loss can be expressed as

$$P_A = \left(\frac{GdwH_0}{\rho} \right)^{1/2} \left(\frac{dB}{dt} \right)^{3/2}, \quad (5.5)$$

where G is a dimensionless constant of value 0.1356, w and d are geometry related dimensions which take 0.19 and 0.0025 here, H_0 has dimensions of Am^{-1} and is equivalent to the external magnetic field.

Incorporation of eddy current loss mechanism into the constitutive relation (3.19) yields a modified hysteresis curve with attenuation in the magnitude of the magnetic

field due to eddy current losses. To satisfy the assumption of homogeneous penetration of the field across the sample, the cylindrical NiMnGa rod is subdivided into thin concentric laminates (Fig. 5.1). For each laminate, the internal free energy considers the dynamic power losses (5.4) and (5.5) has the form

$$G = \psi^{\nu_1} - \frac{1}{2\rho} S_{yy}^{\nu_1} \sigma_y^2 - \xi \frac{\mu_0}{\rho} M_s H - \begin{cases} b_1 \xi + a_1 \xi^2 & \dot{\xi} > 0 \\ b_2 \xi + a_2 \xi^2 & \dot{\xi} < 0 \end{cases} \quad (5.6) \\ + \frac{1}{\rho} \int \frac{\mu_0^2 d^2}{2r\beta} \left(\frac{dM}{dt} \right)^2 dt + \frac{1}{\rho} \int \frac{GdwH_0^{1/2}}{r} \left(\frac{\mu_0 dM}{dt} \right)^{3/2} dt.$$

Substitution of this energy expression into the Clausius-Duhem form of the second law of thermodynamics yields a new expression of the force balance of the system,

$$\pm Y^\xi = \epsilon_s \sigma_y + \mu_0 M_s H_y + \rho \begin{cases} b_1 + 2a_1 \xi & \dot{\xi} > 0 \\ b_2 + 2a_2 \xi & \dot{\xi} < 0 \end{cases} \quad (5.7) \\ - \frac{\mu_0^2 d^2}{2\rho\beta} \frac{d \int \left(\frac{dM}{dt} \right)^2 dt}{d\xi} - \left(\frac{G\mu_0 dw H_0}{\rho} \right)^{1/2} \mu_0 \frac{d \int \left(\frac{dM}{dt} \right)^{3/2} dt}{d\xi}.$$

In [47], the evolution of magnetic magnetization in NiMnGa is discussed based on the thermodynamic framework. Compared with the constitutive model developed in this dissertation, it incorporates the microstructure in the continuum thermodynamics through the use of the internal state variables which include not only the volume fraction ξ , but also the domain fraction α , and the magnetization rotation angle θ (Fig. 5.2). The thermodynamic potentials include the magnetic energy consisting of Zeeman, magnetostatic and anisotropy, and mechanical energy consisting of elastic and twinning components. The constitutive response of the material is obtained by

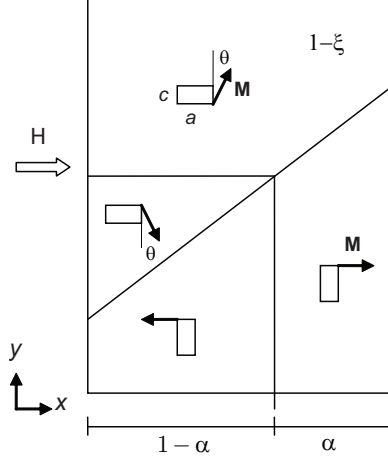


Figure 5.2: Simplified two-variant NiMnGa microstructure incorporating internal state variables.

restricting the process through the second law of thermodynamics. The magnetization of NiMnGa at different values of bias fields is given by

$$M = M_S(2\xi\alpha - \xi + \sin\theta - \xi\sin\theta). \quad (5.8)$$

The expressions for the domain fraction variable α and the magnetization rotation variable θ were shown to have the form

$$\alpha(H, \xi) = \frac{H}{2NM_S\xi_0} + \frac{1}{2}, \quad (5.9)$$

$$\theta(H, \xi, \alpha) = \sin^{-1}\left(\frac{2\mu_0 NM_S^2 \xi \alpha - \mu_0 NM_S^2 \xi - \mu_0 H M_S}{\mu_0 NM_S^2 \xi - 2K_u - \mu_0 NM_S^2}\right) \quad (5.10)$$

respectively. In above equations, parameter N represents the difference in the demagnetization factors along the x and y directions and it is taken as 2.13 by fitting with the experimental data. With the appropriate estimation of the initial condition,

equation (5.7) can be numerically solved with the substitution of α and θ from (5.9) and (5.10).

5.3 Skin Depth Effect

It was already pointed out that the derivation of the constitutive strain model with eddy current and anomalous losses assumes uniform magnetic field penetration through the cross-section of the laminates, so the cylindrical sample was subdivided into many thin concentric laminates to satisfy this assumption. Naturally, the next step of the model development should be the calculation of magnetic field distribution along the radial direction for each laminate. As will be shown soon, for a cylindrical sample, when it is actuated by an alternating magnetic field, the field density tends to be distributed nonlinearly from the surface to its core, this phenomenon is referred to as “skin depth effect”.

5.3.1 Diffusion Equation

The magnetic diffusion describes the magnetic field intensity and phase fluctuations in an electrically conductive material, a partial differential equation will be derived to describe this property for the NiMnGa sample when put in a field parallel to its axial direction. Fig. 5.3 shows the sample and a homogenous applied field along the longitudinal axis of the rod.

From the Ampere’s circuital law, it is known that without external electric potential surrounding the sample, the relationship between the induced current density \mathbf{J}

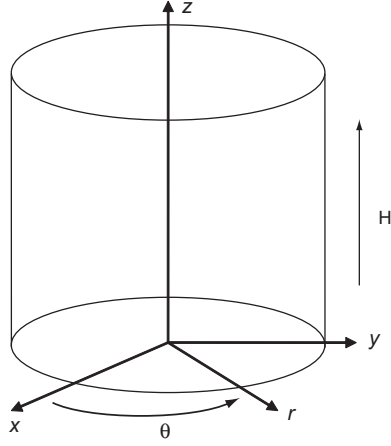


Figure 5.3: Schematic representation of the NiMnGa sample put in a magnetic field parallel to axial direction.

in the NiMnGa sample and the magnetic field \mathbf{H} can be written as:

$$\nabla \times \mathbf{H} = \mathbf{J}. \quad (5.11)$$

Applying the curl operation on both sides yields

$$\nabla \times (\nabla \times \mathbf{H}) = \nabla \times \mathbf{J}, \quad (5.12)$$

while the current density can be written as the electric field divided by the electrical resistivity

$$\mathbf{J} = \frac{1}{\rho} \mathbf{E}. \quad (5.13)$$

Plugging equation (5.13) into (5.22) and applying

$$\nabla \times \mathbf{E} = -\frac{\partial \mathbf{B}}{\partial t}. \quad (5.14)$$

gives the magnetic diffusion equation in the Cartesian coordinates system:

$$\nabla \times (\nabla \times \mathbf{H}) = -\frac{\mu}{\rho} \frac{\partial \mathbf{H}}{\partial t}. \quad (5.15)$$

Transformation from the Cartesian coordinates to the cylindrical coordinates together with the known condition that external magnetic field only has the z -axis component will give the magnetic field diffusion equation in the cylindrical coordinate system.

$$\frac{\mu}{\rho} H_t = \frac{1}{r} (r H_r)_r + H_{zz} \quad (5.16)$$

where t represents the time, r is the radial distance from the center of the cylinder, z is the longitudinal coordinate, and the subscripts denote partial derivatives.

It can also be assumed that the field has a homogenous distribution along the longitudinal axis of the rod, i.e., $H_{zz} = 0$. The distribution of the magnetic field inside the sample can be obtained numerically with the central difference approximation. The result is illustrated in Fig. 5.4. As indicated, there exists not only a phase delay for the magnetic field from the surface to the core, but the magnitude of the magnetic field decreases along the radius as well. The higher the frequency of the external field, the more pronounced the skin depth effect will be.

With the magnetic field at different location along the radius direction, the magnetic field induced strain can be calculated by applying the constitutive strain model (5.6). In the next section, finite element analysis will be provided for the magnetic field and the field induced strain; a coupled magneto-mechanical model will be provided

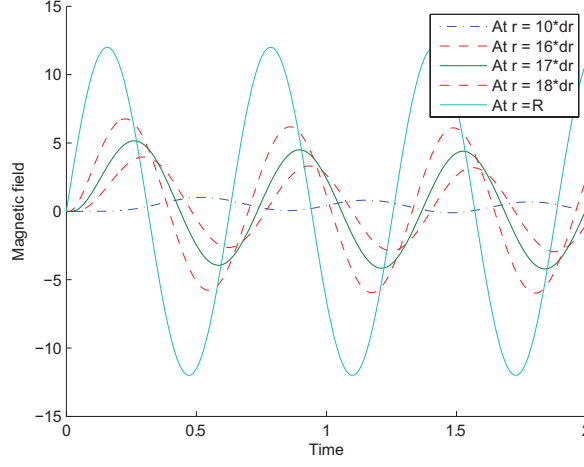


Figure 5.4: Skin depth effect.

using the COMSOL Multiphysics finite element software package and the analytical model in the previous section will be validated.

5.3.2 Finite Element Analysis

In this section, COMSOL will be used to provide the finite element analysis for NiMnGa based transducer. The following subjects will be covered: first, the electromagnetic theory behind the COMSOL magnetic module will be briefly introduced; followed by the development of the magneto-mechanical model; and finally, the simulation of the model will be provided for two different cases, one without the eddy current power loss, the other with the eddy current power loss, the comparison will include:

(1) the magnetic field skin depth effect from the analytical solution and COMSOL solution; and

(2) the magnetic field induced strain from the constitutive model and that from the COMSOL finite analysis.

Electromagnetic Theory

Electromagnetic theory is the basis of operation for electrical generators, induction motors and transformers, etc. It describes the relation between the electric current and magnetism. The classical electromagnetism is summarized by Maxwell with a series of equations known as Maxwell's equations. The equations provide the basis for the study in the following section, in differential form, they are written as:

$$\nabla \times \mathbf{B} = \mathbf{J} \quad (5.17)$$

$$\nabla \cdot \mathbf{B} = 0$$

$$\nabla \times \mathbf{E} = -\mu \frac{\partial \mathbf{H}}{\partial t}$$

$$\nabla \cdot \mathbf{E} = \frac{\rho}{\varepsilon_0},$$

where \mathbf{B} is the magnetic induction, \mathbf{J} is the current density, \mathbf{E} is the electric field, ρ is the electric resistivity, and ε_0 is the permittivity of free space. These equations are also known as the Ampere's circuital law, Gauss's law for magnetism, Faraday's law of induction, and Gauss's law. In the magnetic system of the actuator, the magnetic induction B will be determined first from the time-varying electric current

in the solenoid coil, and the magnetic field intensity \mathbf{H} can be obtained from the constitutive equation

$$\mathbf{B} = \mu\mathbf{H} \quad (5.18)$$

Under certain circumstances it can be helpful to formulate the problem in terms of the magnetic vector potential A , which will be discussed later.

COMSOL Model Definition

A 2-D axis-symmetric module is used in this research, the geometry of the model is shown in Fig. 5.5 where domain D_1 is the NiMnGa sample, D_2 is the solenoid coil,

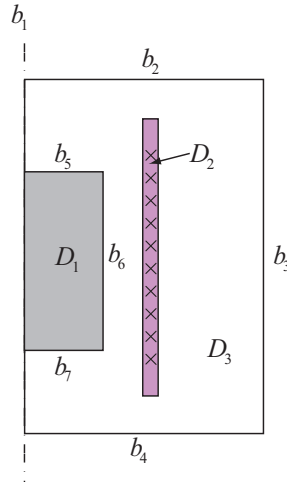


Figure 5.5: Geometry of the model.

and D_3 is the air. The geometry of the sample has a dimension of $0.25 \text{ in} \times 0.9 \text{ in}$,

and it can also be seen that the current in the coil is along the direction into the paper.

The schematic representation of the magnetomechanical transducer system can be found in Fig. 5.6, the magnetic field is described as a function of the external electric current in the solenoid coil, which will be defined in the magnetic module, while the mechanical effects can be described by a series of mechanical variables, and the coupling between these two elements are described by constitutive relations.

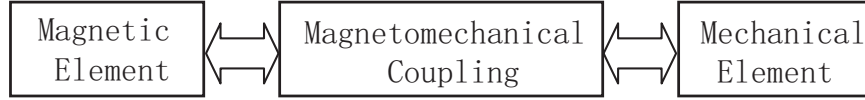


Figure 5.6: A magnetomechanical system.

Domain Equations

The model of magnetic element is built using a 2D axial symmetric “Perpendicular Induction Currents” application mode, and the modeling plane is a cross section of the sample and the surrounding air. The external current density through the cross-section of the solenoid coil is \mathbf{J}^e , while \mathbf{A} is denoted as the magnetic vector potential. The relation that describes the properties of the total current density of the coil is given by:

$$\mathbf{J} = \mathbf{J}^e + \frac{1}{\rho} \mathbf{E}. \quad (5.19)$$

As mentioned before, in electromagnetism, problems can sometimes be formulated in terms of the magnetic potential, for example, the electric field can be formulated in terms of the magnetic vector potential as

$$\mathbf{E} = -\frac{\partial \mathbf{A}}{\partial t}. \quad (5.20)$$

So the total current density can be written as

$$\mathbf{J} = \mathbf{J}^e - \frac{1}{\rho} \frac{\partial \mathbf{A}}{\partial t}, \quad (5.21)$$

While Ampere's circuital law yields

$$\nabla \times \mathbf{B} = \mathbf{J}^e - \frac{1}{\rho} \frac{\partial \mathbf{A}}{\partial t} \quad (5.22)$$

The magnetic induction can also be expressed in terms of the magnetic vector potential

$$\mathbf{B} = \nabla \times \mathbf{A} \quad (5.23)$$

So in the magnetic module, the constitutive equation can be set as

$$\frac{1}{\rho} \frac{\partial \mathbf{A}}{\partial t} + \nabla \times (\mu^{-1} \nabla \times \mathbf{A}) = \mathbf{J}^e. \quad (5.24)$$

After obtaining the magnetic flux density \mathbf{B} , the magnetic field \mathbf{H} can be calculated from equation (5.18).

The mechanical element is modeled using the “2D axial symmetric Stress Strain mode”. For the mechanical module, the dynamic equations of a ferromagnetic shape

memory continuum can be derived from the Hamilton principle, in which the Lagrangian and the virtual work are properly adapted to include the magnetic contributions as well as the mechanical ones, which is in the form of

$$\delta W = \{\delta u\} \cdot \{F^{Mechanical} + F^{Magnetic}\}.$$

The potential energy density of FSMA material includes contributions from the strain energy and from the magnetic energy, which are in the forms of

$$E_{Potential} = \frac{1}{2} \{\mathbf{S}\} \cdot \{\boldsymbol{\sigma}\} + \int \mathbf{H} \cdot d\mathbf{B}$$

substitution of the potential and virtual work δw into the Hamilton principle will yield the dynamic equations for each element in the form of [13]

$$m \frac{d^2 u_i}{dt^2} + \xi \frac{du_i}{dt} + k u_i = f(t). \quad (5.25)$$

Boundary Conditions

To get a full description of the electromagnetic problem, appropriately specified boundary conditions have to be defined for interface between materials and physical boundaries. For the magnetic module, boundary “b1” in Fig. 5.5 is known to be “axis symmetric”, while “b2” and “b4” can be defined as magnetically insulated boundaries. Since “b5” to “b7” are the internal boundaries in this module, the continuity conditions will be satisfied automatically. For the interfaces between different media in the model, they are subjected to the condition

$$\mathbf{n} \cdot (\mathbf{B}_1 - \mathbf{B}_2) = 0 \text{ and } \mathbf{n} \cdot (\mathbf{H}_1 - \mathbf{H}_2) = 0$$

where \mathbf{n} is the normal direction of the interface, and $\mathbf{H}_1, \mathbf{H}_2, \mathbf{B}_1, \mathbf{B}_2$ are the magnetic field and flux density in adjacent materials.

In the mechanical boundary settings, the boundary "b7" is fixed and the symmetric axis can only deform along the z-axis. It should be noted that when constructing the system equations, each element of the mesh is connected to its neighboring elements at the global nodes and the displacement is continuous from one element to the next.

Simulation Results

With the properly set boundary conditions, simulation of the model can be run with the right meshing process. Since COMSOL can detect areas with high rate of change of stresses and magnetic field, the default meshing settings are used here.

First, the comparison of the magnetic field from the analytic model and COMSOL simulation is provided. The solution from the finite element analysis is plotted in Fig. 5.7, it shows the magnetic field distribution at different instant of time. It is observed that indeed, due to the skin depth effect, the magnetic field is nonuniform inside the sample.

To be more specific, four points from the center of the sample to the surface ($r = 0, r = 0.33R, r = 0.66R$, and $r = R$) are picked to show the magnetic field evolution at these points. As results from the analytic equation (5.16), it is shown in Fig. 5.8 that from the surface to the core of the rod, there is not only a decay for the magnitude of the field, but there exists a phase delay as well.

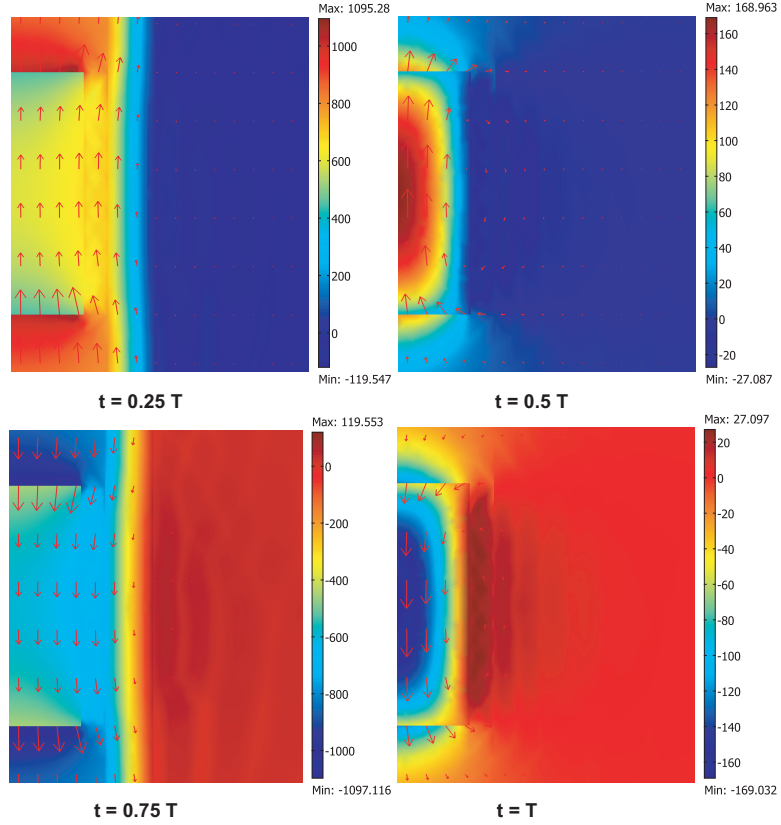


Figure 5.7: Magnetic field distribution in one cycle.

In general, when solving the analytic diffusion equation, the assumption of the field independence along the longitude direction is applied, physically that means the sample is assumed to be infinitely long, which can not be true in reality. Now the length dependence will be shown with simulation by using NiMnGa samples with different lengths. In implementation, two simulations were run on a sample of 0.8 inch long and the other of 8 inch long. The solution for these two cases are shown in Fig. 5.9.

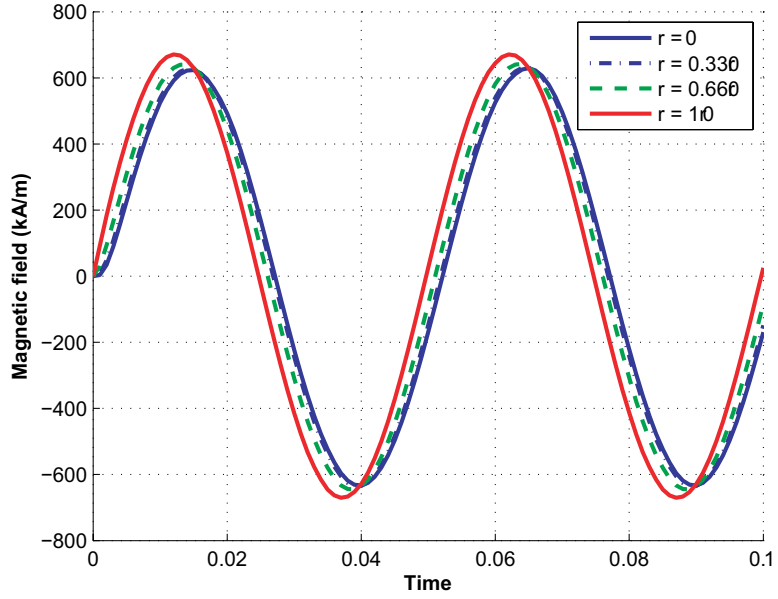


Figure 5.8: Magnetic field at different locations from the center to the surface of the sample.

To quantify the difference of these two cases, the mean square error is calculated between the analytic result and COMSOL result, which is listed in Table 5.1. The external magnetic field in COMSOL simulation is used as the boundary condition solving the analytic model, so the error at the surface is always 0 for both cases. However, at other locations inside the sample, it can be seen that the longer sample has a smaller mean square error compared with the sample with short length, which indicates that the error can not be ignored for short samples when calculating the field using the diffusion equations.

With the power losses in dynamic situations, the frequency dependence on the field induced strain can also be shown in FEM analysis; due to the assumption of uniform

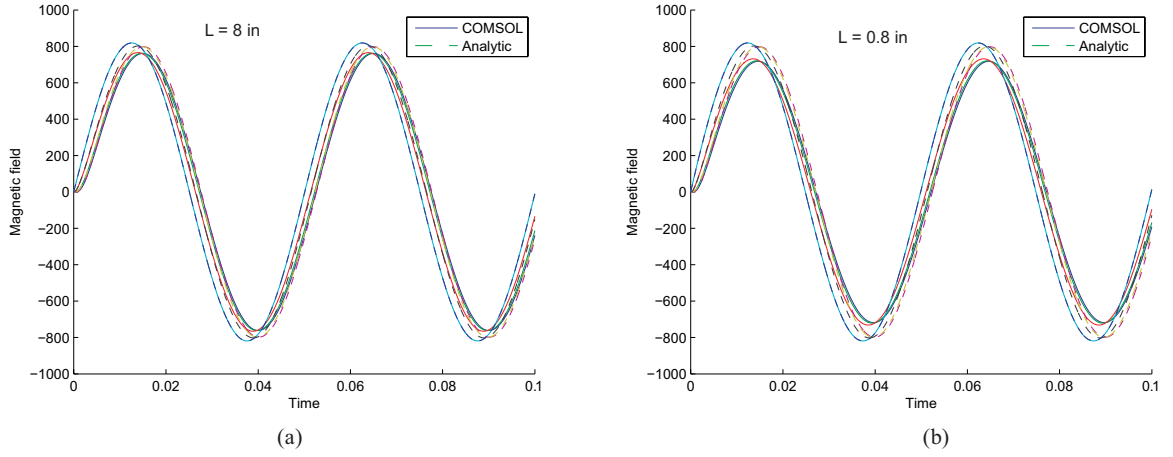


Figure 5.9: Comparison of magnetic field at different locations between COMSOL result and analytic result: (a) Sample length = 0.8 in. (b) Sample length = 8 in.

Length (in)	$r = 0$	$r = 0.33R$	$r = 0.66R$	$r = R$
0.8	7.25%	7.03%	6.4%	0
8	2.32%	2.3%	2.3%	0

Table 5.1: Error at different locations between analytic result and COMSOL result for samples with different lengths

field penetration when considering the power loss, the field induced strain should be compared for all the concentric laminates with different radius, for simplicity, only the strain at the center of the rod is considered. Applying the driving field with different frequencies, it can be seen from Fig. 5.10 that the result from constitutive model (5.7) and that from COMSOL have a good match, with the increase of the frequency, the maximum of the field induced strain is getting smaller, which means the higher the driving frequency, the more energy will be dissipated as heat.

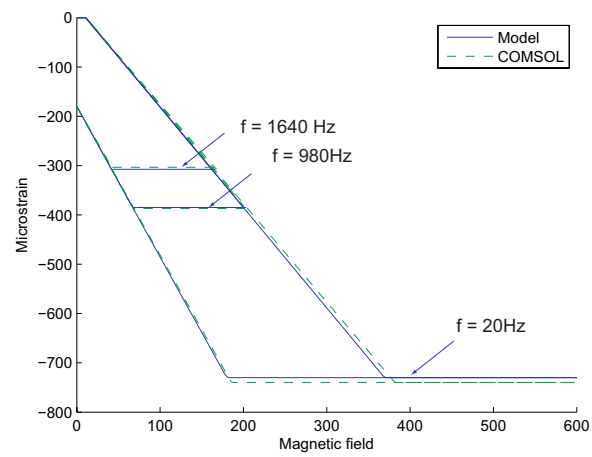


Figure 5.10: Comparison of field induced strain between the constitutive model and COMSOL with eddy current power loss.

CHAPTER 6

EFFICIENCY ANALYSIS

6.1 Introduction

The energy characteristics of a NiMnGa based actuator is studied in this Chapter, the approach provided will be useful for designing an energy efficient actuating system. Following the ideas taken by previous literatures[21, 22, 33] about the efficiency analysis on other smart material actuators, the energy delivery efficiency and energy conversion efficiency for the NiMnGa actuator will be defined first, and the calculations of these efficiencies based on a linear constitutive model and a nonlinear model are discussed. The optimal stiffness ratio, which is defined by the ratio of external spring stiffness with respect to the internal actuating element stiffness and at which the efficiencies reach the maximum, can be obtained analytically for the linear model, while numerical techniques have to be used for the nonlinear model. To verify the validity of the calculation of optimal stiffness from the constitutive model, experiments are run on a rectangle NiMnGa specimen using the conventional perpendicular field-stress configuration. Since it is impracticable to test the spring with stiffness

ranging from zero to infinity, eight different springs with stiffness around the calculated optimal stiffness rate are tested. The measured energy efficiencies are compared with the theoretical results and the discussion is provided at the end of the chapter.

6.2 Analytical Approach

The use of smart material actuators has been greatly expanded in recent years, these actuators transform the input electrical energy into output mechanical energy. The power and energy characteristics of these smart materials have been studied by Leo and Giurgiutiu[21, 22, 33]. The literatures consider the one-directional operation of the induced strain actuators of Piezoelectric (PZT), electrostrictive (PMN) and magnetostrictive (Terfenol-D) actuators against the external loading system. It is found that the maximum energy output from these actuators is obtained when the internal and external stiffnesses are matched, here the output energy is defined as the energy delivered by the active material into the external system. They also confirm that the electromechanical conversion efficiency reaches the maximum at the stiffness match point by tests on commercially available actuators. This dissertation will extend their methodology to the ferromagnetic shape memory alloy NiMnGa by analyzing the energy delivery efficiency and the energy conversion efficiency for NiMnGa actuators. As the starting point, this dissertation will focus on quasi-static situations.

6.2.1 Definitions

The definition of the energy delivery efficiency is given by:

$$\eta^{\text{delivery}} = \frac{\text{Energy delivered to the external load}}{\text{Load-free reference energy in transducer}}$$

while the energy conversion efficiency considers how much input electric energy is converted and transferred to the external system, hence, it is defined as:

$$\eta^{\text{conversion}} = \frac{\text{Energy delivered to the external load}}{\text{Input electrical energy}}.$$

In real applications, actuators usually work in one-directional operation; and although most of them have the nonlinear constitutive relationship between the induced strain and external stimulus such as electric field, magnetic field or mechanical stresses, for simplicity purposes, all literatures assume the active devices work in their linear region, and the classical linear constitutive model has the form of

$$\begin{aligned}\varepsilon &= S\sigma + dH \\ B &= d\epsilon + \mu H\end{aligned}\tag{6.1}$$

where ε, B denote the induced strain and magnetic flux density, while S is the mechanical compliance of the active materials, d is the piezomagnetic coefficient, and μ is the magnetic permeability.

This dissertation will express these two efficiencies based on the linear constitutive model, then apply the nonlinear phenomenological NiMnGa model developed by Sarawate[47] to calculate the optimal stiffness ratio for the NiMnGa.

6.2.2 Analytic Expressions

Due to that only quasi-static situations are considered in this disertation, the inertial and damping effects of the actuator are ignored, so the system is simplified to consist of only an actuating element working against a spring load, which is a general way taken in other works [20, 21, 23, 33]. The schematic representation of the actuator system is shown in Fig. 6.1.

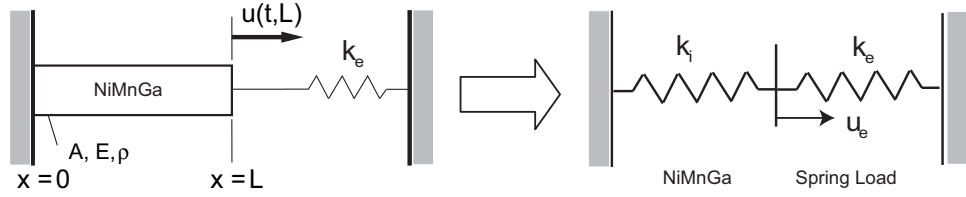


Figure 6.1: Schematic representation of a simplified transducer.

The load-free deformation of the transducer can be assumed to be u_0 , and after an external spring load is added to the system and working against the active element, the total induced strain displacement u_0 should have the relation:

$$u_0 = u_i + u_e \quad (6.2)$$

where u_i and u_e denote the internal and external displacements; this simple analysis reveals that the total induced-strain displacement is partly consumed as an internal displacement due to the compressibility of the actuating element and partly delivered as a useful output displacement. Since the elements are connected in series, the magnitude of the force applied to each should be the same, it is not difficult to get

$$u_i = \frac{k_e}{k_i} u_e, \quad (6.3)$$

substitution of equation (6.3) into equation (6.2) yields

$$u_e = \frac{1}{1 + k_e/k_i} u_0 = \frac{1}{1 + r} u_0 \quad (6.4)$$

with $r = k_e/k_i$ as the stiffness ratio.

In the actuator, the NiMnGa element is driven by the magnetic field created from the electromagnet, with the direction perpendicular to the longitude direction of the sample. The electric circuit of the actuator consisting of the coil can be simplified to be a pure inductor driven by a current power supply. To get the expression of energy conversion efficiency, the equivalent inductance of the coil has to be obtained. Following the same method as Leo [33] used to define the equivalent capacitance for piezoelectric actuators, the equivalent inductance of the electromagnet coil can be derived with the assumption of linear deformation of active materials in a certain region. The second equation in (6.1) can be rewritten as:

$$B = -d\frac{F}{A} + \mu H. \quad (6.5)$$

The only external force F is from the reaction of the spring load, which can be expressed as the product of the deformation and the spring stiffness, i.e., $F = k_e u_e$.

Substitution of this expression and equation (6.4) into equation (6.5) gives

$$B = \mu(1 - \frac{d^2}{s\mu} \frac{r}{1+r})H = \mu^* H. \quad (6.6)$$

Consequently, the equivalent inductance becomes

$$\begin{aligned} L^* &= \frac{\mu^* N^2 A}{l} = L(1 - \frac{d^2}{s\mu} \frac{r}{1+r}) \\ &= L \left(1 - \kappa^2 \frac{r}{1+r} \right) \end{aligned} \quad (6.7)$$

where $\kappa^2 = \frac{d^2}{s\mu}$ is defined as the coupling coefficient.

The dissipated energy from the power supply can be defined as the energy stored in the inductor, which is written in the form of [19]:

$$E_{elec}^{linear} = \frac{1}{2} L^* I^2, \quad (6.8)$$

while the output energy for a linear system can be defined as half the product between force and output displacement

$$E_{out}^{linear} = \frac{1}{2} k_e u_e^2 \quad (6.9)$$

which can be further rewritten as

$$E_{out}^{linear} = \frac{1}{2} \frac{r}{(1+r)^2} k_i u_0^2. \quad (6.10)$$

Combining (6.7)(6.8)(6.10) will give the expression of energy conversion efficiency for a linear constitutive model:

$$\eta_{conversion}^{linear} = \frac{\frac{r}{(1+r)^2}}{1 - \kappa^2 \frac{r}{1+r}}, \quad (6.11)$$

while the energy delivery efficiency can be expressed as

$$\eta_{delivery}^{linear} = \frac{\frac{1}{2} k_e u_e^2}{\frac{1}{2} k_i u_0^2} = \frac{r}{(1+r)^2}. \quad (6.12)$$

Equation (6.11) and equation (6.12) give the efficiency definitions for the actuator with the linear constitutive model. Taking the derivative of these two efficiencies with respect to the stiffness ratio, the theoretical optimal stiffness ratios can be obtained as

$$\begin{aligned} r_{delivery}^* &= 1 \\ r_{conversion}^* &= 1/\sqrt{(1 - \kappa^2)}. \end{aligned}$$

It is worth noting that the optimal stiffness ratio for energy delivery, $r_{delivery}^*$, and that for the energy conversion, are different. In application design, either of the two efficiencies can be optimized, but not both. In other words, one can either design for maximum energy output by choosing the stiffness ratio of 1, or can design for

maximum conversion efficiency by choosing $r = 1/\sqrt{1 - \kappa^2}$. However, for practical applications, since κ^2 is usually much smaller than 1, the numerical difference between the two results is small and can be ignored.

For the optimal stiffness ratio just derived, the intrinsic nonlinearity of NiMnGa performance limits its accuracy with linear assumptions. To address this problem, the model is extended by replacing the linear constitutive model with a nonlinear one. As mentioned, the conventional perpendicular driving configuration will be used for the experimental validation, so a nonlinear constitutive model for the field induced strain and magnetization developed by Sarawate [47] is used in the calculation. Together with the transducer model developed in Chapter 4, the conversion efficiency and delivery efficiency from the integration using trapezoidal rule can be obtained as:

$$\eta_{delivery}^{nonlinear} = \frac{\int k_e u_e du_e}{\int k_i u_0 du_0} \quad (6.13)$$

$$\eta_{conversion}^{nonlinear} = \frac{\int k_e u_e du_e}{\int L^* I dI} \quad (6.14)$$

in which u_0 and u_e are the deformations when there is no loading and when the actuator is connected with a spring load; they can be calculated from the constitutive model in [47]. The model simulation of the efficiencies versus the stiffness ratio will be provided together with the experimental results in the next section.

6.3 Experimental Validation

Having obtained the expressions for the analytic conversion and delivery efficiencies, experimental data of actuation need to be provided to verify the validity of

the solutions. To that end, a custom made electromagnet is used and the schematic representation of the setup is shown in Fig. 6.2. The whole system consists of an electromagnet and a spring as the restoring system. To calculate the conversion efficiency, the inductance of the coil has to be determined first.

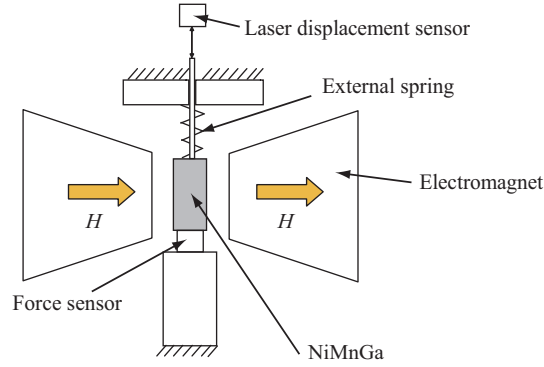


Figure 6.2: Experimental setup.

6.3.1 Coil Characterization

Inductance is an effect which results from the magnetic field that forms around a current-carrying conductor, it is a measure of the amount of electromotive force (EMF) generated for a unit change in current. For a solenoid coil, the inductance can be calculated through the equation:

$$L = \mu N^2 A / l, \quad (6.15)$$

where μ is the permeability of the material within the solenoid, A is the cross-section area, N is the number of turns, and l is the length of the coil.

However, the inductance of the coil can also be determined experimentally from the relation

$$Z = Z_R + Z_L \quad (6.16)$$

where Z is the impedance of the circuit, Z_R and Z_L represent its resistance and inductance components. When the frequency of the circulating current is high enough, Z_R will become so small compared to Z_L that it can be ignored and the total impedance is approximated to be a linear function of the frequency due to the relation $Z_L = j\omega L$, the inductance can be estimated by measuring the slope of the impedance curve with respect to the frequency.

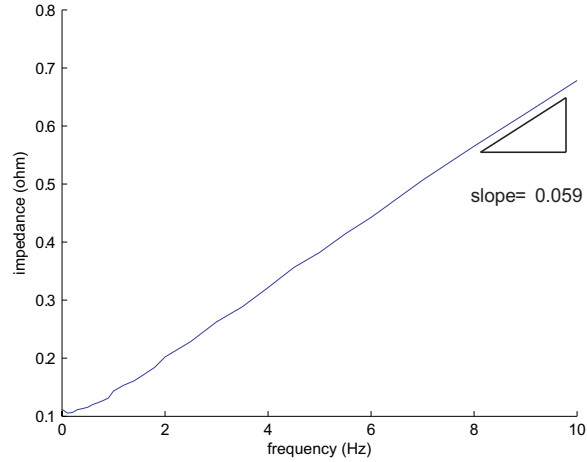


Figure 6.3: Impedance versus frequency in the coil characterization.

In the experiment, sinusoidal excitations with thirty frequencies ranging from 0 to 10 Hz are applied to the coil and the impedance versus frequency of the coil is shown in Fig. 6.3. It can be seen that when the driving frequency goes above 5 Hz, the

resistance component has almost no contribution to the total impedance any more, and the slope of the curve is measured to be 0.059 ohm·s, so the inductance of the coil can be determined by:

$$L = \frac{0.059}{2\pi} = 0.0094 \text{ Henry}$$

6.3.2 Actuation Test

With the measured coil inductance, the stored electric energy can be calculated, which will be further used as the input electric energy in the definition of the energy conversion efficiency. Next, eight different springs will be used to obtain the deformation response of NiMnGa actuator and verify the validity of the efficiency model built in previous section.

A 6mm×6mm×8.9 mm AdaptaMat single crystal NiMnGa sample is placed in the center of the electromagnet. The sample is first converted to a single variant structure by applying a compressive force along the longitude direction, the spring is then installed against the sample. The orthogonal magnetic field is provided by the electromagnet with a sinusoidal input signal of 0.1 Hz frequency and 22.1 volts magnitude (the specifications of the electromagnet can be found in the Appendix). The current is measured by the current monitor in the Techron 770 Amplifier. The displacement is measured by a Keyence Laser Sensor. This procedure is repeated for springs with different stiffness rates.

The effective internal stiffness rate of the NiMnGa can be obtained from previous characterization test on another AdaptaMat sample with the same composition [47]. From Fig. 6.4, the Young's Moduli of NiMnGa in the elastic and detwinning regions are found by the data-fitting to be 92.57MPa and 14.99 MPa. The sample tested has a cross-section area of 36 mm² and the length of 8.76 mm, the corresponding equivalent stiffness can be calculated as 61602.74 N/m and 552452.05 N/m, or 1567.3 lbf/in and 351.76 lbf/in respectively.

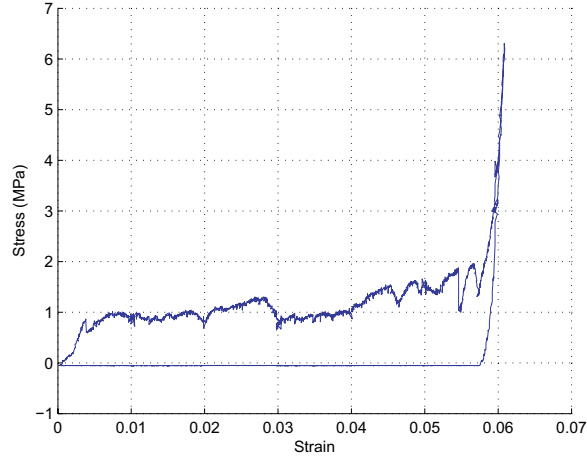


Figure 6.4: Stress-strain curve for AdaptaMat NiMnGa sample.

From the experiments, the magnetic field induced deformation can be obtained for the load-free and other cases with the spring loading. Applying equation (6.13) will give the experimental energy conversion efficiency and the energy delivery efficiency. The final results are listed in Table 6.1, in which r is the stiffness ratio, and η represents the efficiency.

Spring rate (lbf/in)	Stiffness ratio r	Conversion η	Delivery η
132	0.37	9.24%	18.19%
210	0.59	14.74%	20.97%
303	0.86	28.31%	32.93%
357	1.01	29.03%	36.73%
395	1.12	29.25%	35.17%
417	1.18	27.84%	33.34%
486	1.38	25.08%	31.09%
785.4	2.23	18.48%	21.4%

Table 6.1: Conversion and delivery efficiencies for springs with different stiffness rates

The results are also summarized in the following figures, which show the energy conversion efficiency and energy delivery efficiency as functions of the stiffness ratio from analytic models and experimental data.

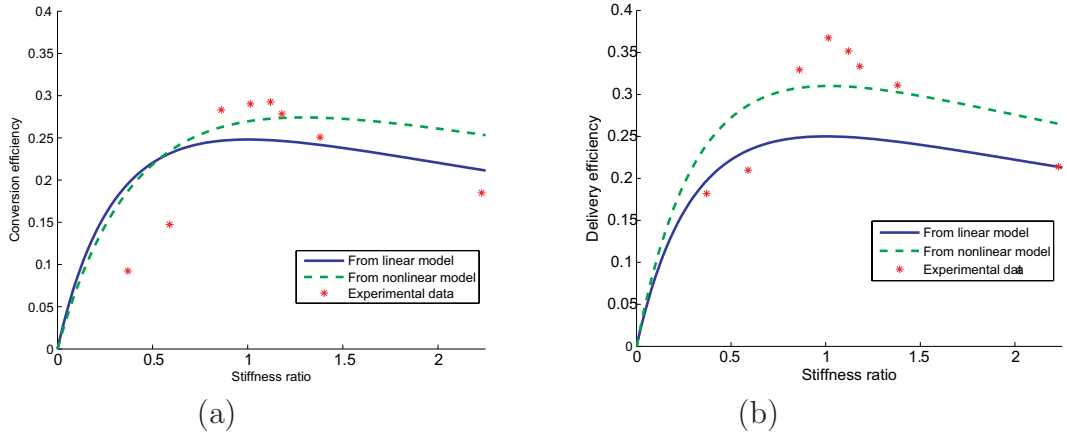


Figure 6.5: (a) Energy conversion efficiency; (b) Energy delivery efficiency

In Fig. 6.5 (b), the maximum energy output was found to exist when the external stiffness and the internal stiffness of the actuator matches ($r = 1$) from both linear

and nonlinear model. This is also verified by the experimental result, in which the maximum happens at $r = 1.01$; as for the electromechanical conversion efficiency of the transducer, it is found that the maximum efficiency takes place at $r = 1.02$ for linear model, while at $r = 1.28$ for nonlinear model, the experiment yields the optimal stiffness ratio as $r = 1.12$. It is worth noting that, with the increase of the external spring stiffness, the field-induced-deformation is getting smaller from (6.4), which means the increase of the efficiency is at the expense of the field induced deformation. When the stiffness ratio is close to zero, although the MFIS is getting close to the maximal strain capability, which is 6% for tetragonal NiMnGa structure, both the delivery efficiency and conversion efficiency are approaching zero. Beyond the optimal stiffness ratio, these efficiencies also go to zero because of the rapid decay of the actuator deformation.

CHAPTER 7

CONCLUSIONS AND FUTURE WORK

7.1 Conclusions

This dissertation has three contributions. The first is the modeling of the FSMA NiMnGa based transducer with the collinear field-stress driving mechanism. The second is to extend the quasi-static transducer model by incorporating the dynamic power loss. And the last contribution is to provide an parametric analysis of the NiMnGa actuator performance based on its energy delivery efficiency and energy conversion efficiency. These three contributions provide a complete method for design an efficient actuator in real applications.

In Chapter 3, a phenomenological constitutive model was developed from the thermodynamics framework. In this model, the internal bias stresses from pinning sites in the material provide the restoring force which allows for the reversibility of the strain. First, the Gibbs free energy for a simplified two variants structure was defined in terms of the external independent state variables of stress, magnetic field, together with the internal state variable of the twin variant volume fraction. The evolution

of the volume fraction is then obtained by applying the first and the second law of thermodynamics. Stochastic homogenization is also used to account for variability in the bias stresses throughout the material and inhomogeneity in the interaction field intensity.

Chapter 4 modeled the internal rod dynamics through force balancing with boundary conditions dictated by the constructive details of the transducer and mechanical load. The model is formulated in variational form, resulting in a second-order temporal system with magnetic field induced strain as the driving mechanism.

Chapter 5 extended the quasi-static transducer model by incorporating the dynamic power loss which includes the eddy current loss and the anomalous loss. Following the idea of Bertotti [1, 2, 3, 4, 5] that the dynamic loss is associated with the macroscopic large-scale behavior of the magnetic domain structure, the eddy current loss and anomalous loss is defined to be dependent on the rate of change of the magnetic induction through the cross-section of the material. Hence, the quasi-static hysteresis curves can be extended to a more general frequency dependent model.

In Chapter 6, the energy characteristics of the transducer were studied, expressions for the energy delivery efficiency and energy conversion efficiency as functions of the stiffness ratio were derived, which are based on the relationship among the energy delivered to the external load, energy created by the transducer with free-load and the energy stored in the inductor as the input electrical energy. The efficiency analysis provides optimal stiffness ratios for the maximum energy conversion and maximum

energy delivery. This study can be used for designing an energy efficient control system and will facilitate the development of this new class of transducers.

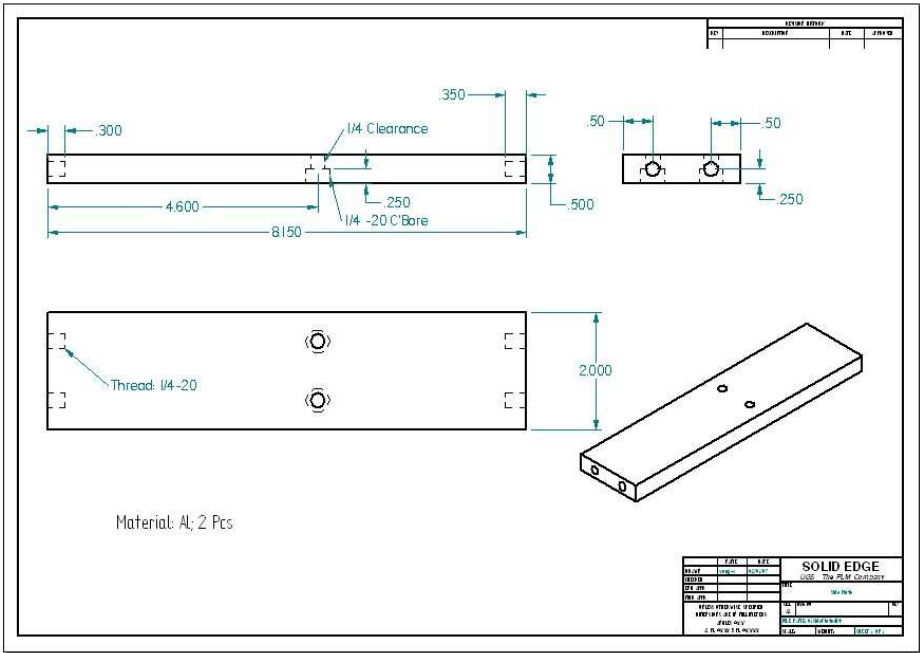
7.2 Future Work

Although rapid progress in the development of smart materials based transducers has been made recently, for collinear stress-field driven NiMnGa transducers, there is still a long way to get widely accepted. Following the line of this dissertation, some research topics to be addressed are listed below.

1. Further microscopic investigations should be done to provide the understanding of the pinning mechanism, including the effect of heat or stress treatment on the negative side from pinning sites, such as inactivity of NiMnGa element caused by the too strong internal stresses. This will facilitate the manufacturing of the active NiMnGa specimen to be used in the transducer.
2. The benefits of the NiMnGa are high strains and the broad bandwidth, which enable robust and simple design of the actuator. However, hysteresis of the NiMnGa can be a problem in some control applications. So in position control applications, advanced control algorithms can be designed to address this problem.

APPENDIX A

EFFICIENCY TEST DEVICE DRAWINGS



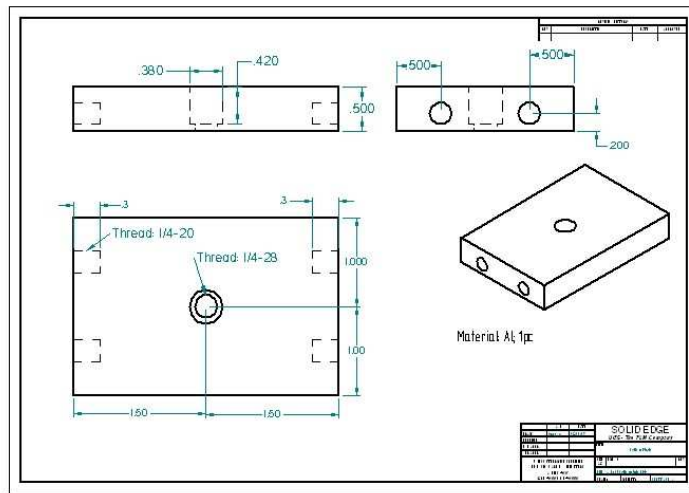


Figure A.3: Bottom plate.

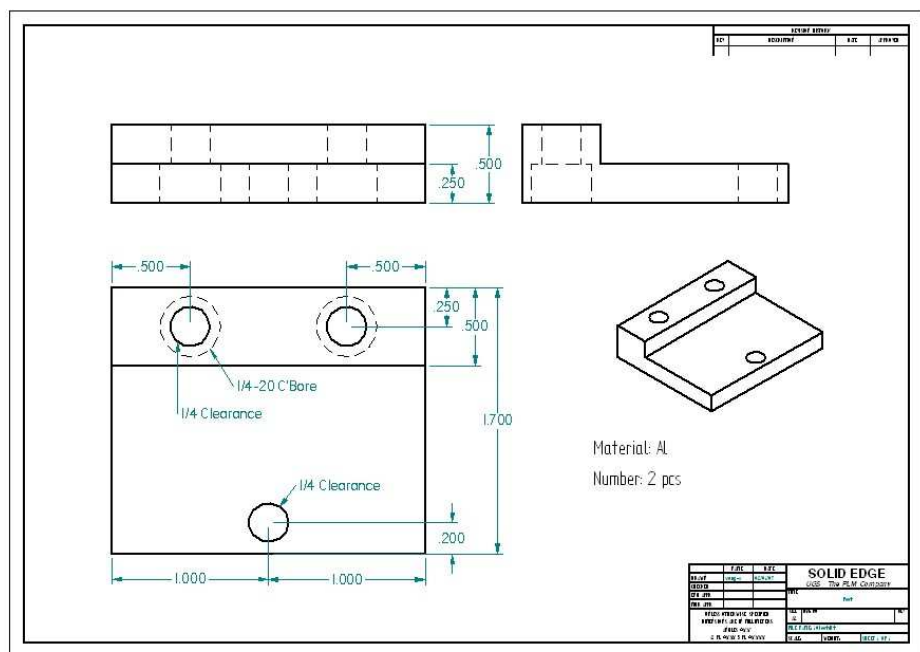
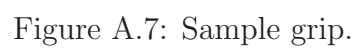


Figure A.6: Fixture feet.



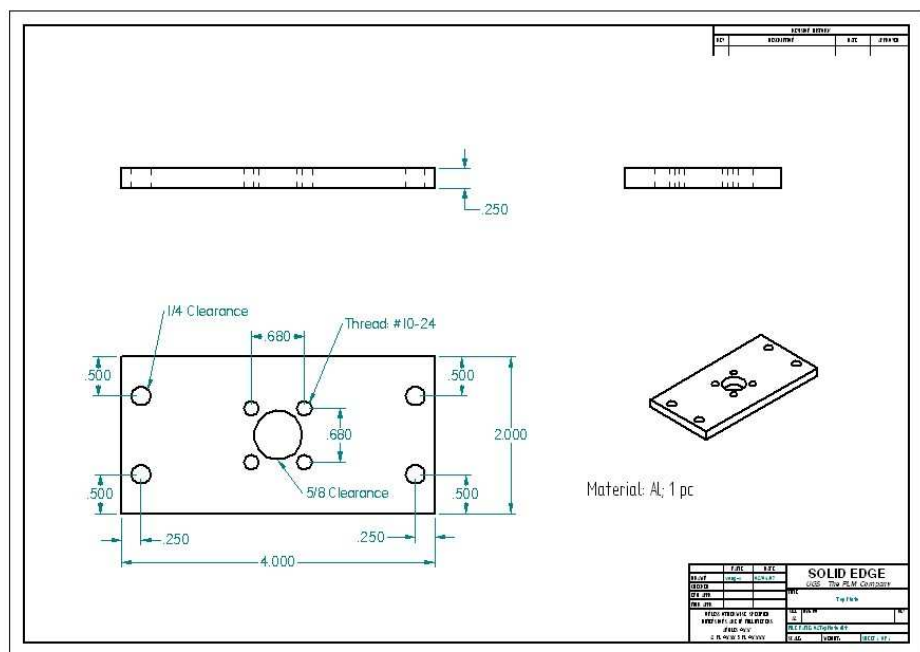


Figure A.8: Top plate.

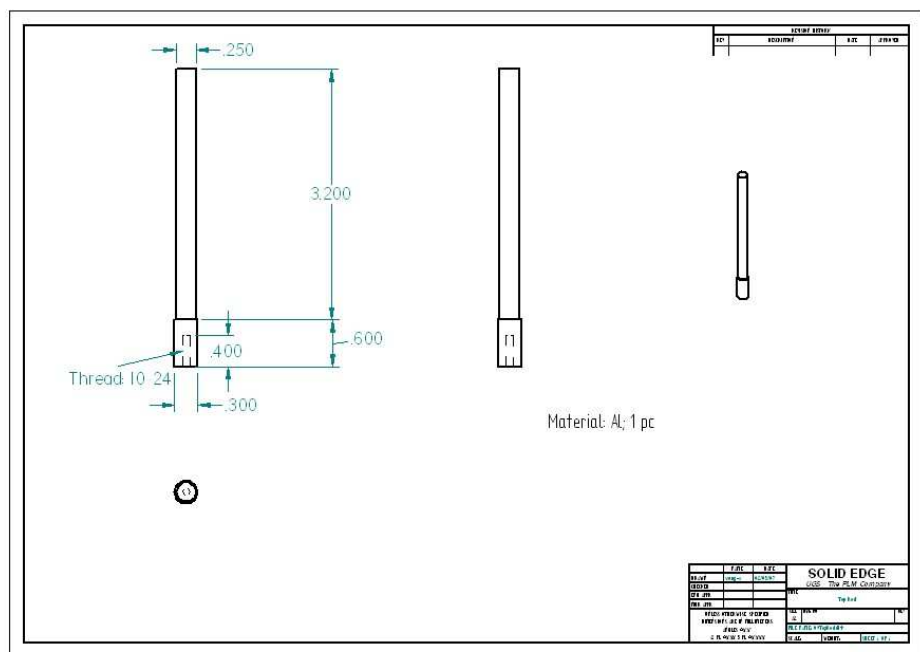


Figure A.9: Upper rod.

APPENDIX B

FIELD INDUCED STRAIN VERSUS CURRENT

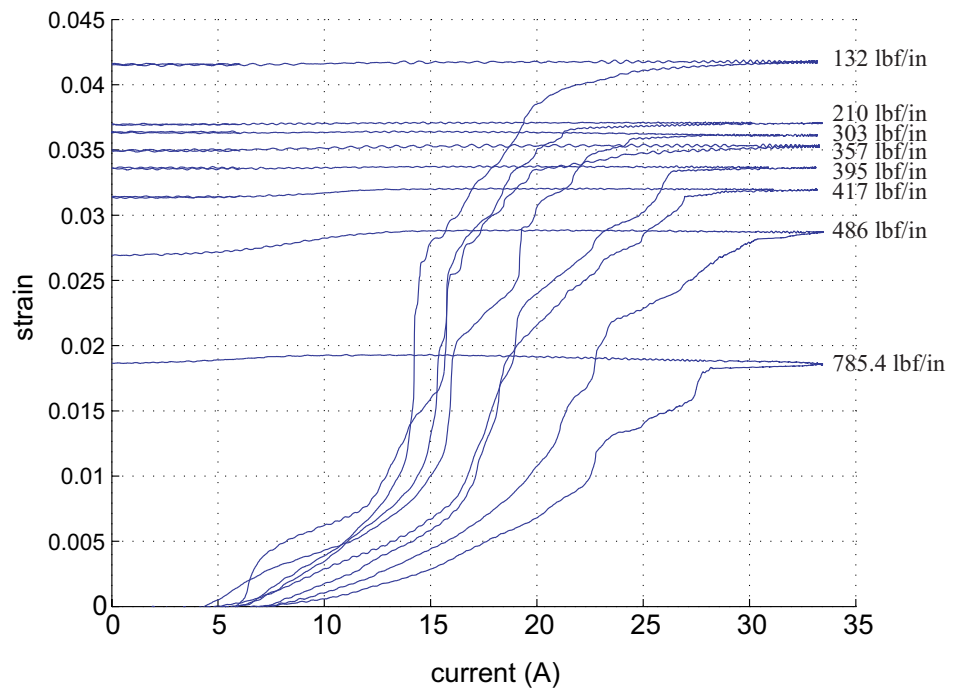


Figure B.1: Field induced strain versus current.

APPENDIX C

CODE

C.1 Volume Fraction Evolution Function

```
function eps_mod = xi_bar_v(H,H_next,Hi,k2,sigma,eps_s,n,K)
% Define Coefficients
S=0;
mu_0 = 1.256e-006; %NA^-2
Ms = 622000; %Am^-1
rho=1;
Y= 209570;
eps_th = -60000e-6;
H1 = 10750; % average of measured values
eps_2 = -5.7612e-023*sigma^3 - 4.0960e-016*sigma^2 + ...
-8.5320e-010*sigma -6.3526e-004; % 3rd order fit (only 4 data points)
slope=H_next-H;
Hy=H+Hi;
[Hy_m,k2_m] = meshgrid(Hy,k2);
c1 = eps_s.*sigma + 1/2*S.*sigma.^2 + mu_0*Ms*H1 - Y;
c2_m = eps_s.*sigma + 1/2*S.*sigma.^2 + Y - 2*k2_m.*eps_2./eps_th;
k1_m=n.*k2_m;
xi_s = eps_s/eps_th;
xi1 = (slope>=0).*(1./(2.*rho.*k1_m).*(eps_s*sigma + .5*S*sigma^2 + ...
mu_0.*Ms.*Hy_m-rho*c1-Y + K.*Hy_m))+ (slope<0).*(1./(2.*rho.*k2_m)...
.*(eps_s*sigma+.5*S*sigma^2+mu_0.*Ms.*Hy_m-rho.*c2_m+Y + K.*Hy_m));
xi = (xi1<xi_s).*xi1 + (xi1>xi_s).*xi_s;
eps_mod = eps_th.*xi;
```

C.2 Piecewise Stress-Strain Fitting Function

```
function pp = stress_strain
```

```
% This function find the piecewise continuous polynomial fit to the the
% stress vs maximum strain data for our sample. It is designed to be used
% with FEmodel.
```

```
eps = [4.1000
2.1455 %2.1170
1.8158 %1.7776
1.5743 %1.5572
1.2416
0.9617
0.7295
0.6282
0.5508
0.4794
0.4020
0.3543
0.2650
0.2174
0.1816
0.1638
0.1399
0.1280
0.0983
0.0863
0.0744
0.0804
0.0625
0.0625
0.0506]*-10^-3;
```

```
sigma = [0.0121
0.13 %0.1551
0.27 %0.2792
0.41 %0.4033
0.6515
0.9617
1.7684
2.6370
3.4436
4.1262
4.9328
5.5533
7.1044
8.5315
9.8345
11.2616
12.7508
14.0538
16.9080
19.7001
27.8904
31.3030
34.5295
51.4685
58.1696]*-10^6;
```

```
pp = pchip(sigma,eps);
temp1 = [-60e6:1000:0];
```

C.3 Constrained Optimization Function

```

% Constrain Optimization for the FEmodel
% Case
tic
fun = @Fun_tot_opt;
const = @my_const;
% Set initial guesses & bounds for constrained parameters
n_i = 1.2; % initial guess for n (1.27
n_u = 2; % upper bound on n (2,
n_l = 1; % lower bound on n (1,
k_bar_i = 1; % *10^6 initial guess for k_bar (1.32e6
k_bar_u = 3; % *10^6 upper bound to k_bar (3e6
k_bar_l = .5; % *10^6 lower bound to k_bar (.7e6
c_i = .4;
c_u = 1;
c_l = .1;
b_i = 2;
b_u = 5;
b_l = .01;

ub = [n_u,k_bar_u,c_u,b_u];
lb = [n_l,k_bar_l,c_l,b_l];
x0 = [1, .5, .83083, 2.5556];
[x,fval] = fmincon(fun,x0,[],[],[],[],lb,ub,const);
fval

format short g
x
toc

```

C.4 Mean Square Error Calculating Function

```

function f = Fun_tot_opt(x)
for dc = 1:4 % Data for Case
    % Evaluate Model with these parameters
    [eps,H] = FEmodel_val(x,dc,'r');
    case
        [eps_d,H_d] = dat_fun(dc);
        % Calculate Error
        i1 = find(eps_d==0);
        i2 = find(H==max(H));
        %————— Absolute Value of the Difference
        err = abs(eps(i1:length(eps_d))-eps_d(i1:length(eps_d)))';
        err_tot(:,dc) = mean(err);
    end
end

```

```
f = sum(err_tot);
```

C.5 Legendre Points and Weights Calculating Function

```
function [x,w] = Legen_xw(a,b,n,nInt)
% Purpose: Finding Legendre points and weights
% Synopsis: [x,w] = Legen_xw(a,b,n,nInt)
% a: lower limit of x
% b: upper limit of x
% n: the order of the Legendre polynomial
% nInt: the number of subintervals
% Written by: Xiang Wang @ 12/12/2005

pbb = [1];
if n==0
    p = pbb; return;
end

pb = [1 0];
if n == 1
    p = pb; return;
end

for i = 2:n
    p = ((2*i-1)*[pb,0]-(i-1)*[0,0,pbb])/i;
    pbb = pb; pb = p;
end

xTemp = roots(p)'; xTemp = sort(xTemp);
for j = 1:n
    y = zeros(1,n);
    y(j) = 1;
    p = polyfit(xTemp,y,n-1); P = poly_itg(p);
    wTemp(j) = polyval(P,1) - polyval(P,-1);
end

lenSub = (b-a)/nInt;
aTemp(1) = a; bTemp(1) = a+lenSub;
for i = 2:nInt
    aTemp(i) = aTemp(i-1)+lenSub; bTemp(i) = bTemp(i-1)+lenSub;
end

for i = 1:nInt
    x((i-1)*n+1:i*n) = (aTemp(i)+bTemp(i))/2+xTemp*(bTemp(i)-aTemp(i))/2;
    w((i-1)*n+1:i*n) = wTemp*(bTemp(i)-aTemp(i))/2;
end
```

C.6 Kernel Calculating Function

```
function gk = good_kern(Hi,k2,n,sigma,eps_s);
H = 700e3;
```

```

S=0;
mu_0 = 1.256e-006; %NA^-2
Ms = 622000; %Am^-1
rho=1;
Y= 209570;
eps_th = -60000e-6;
H1 = 10750; % average of measured values
eps_2 = -5.7612e-023*sigma^3 + -4.0960e-016*sigma^2 + ...
-8.5320e-010*sigma + -6.3526e-004;
K = 0;
Hy=H+Hi;
[Hy_m,k2_m] = meshgrid(Hy,k2);
k1_m=n.*k2_m;
c1 = eps_s.*sigma + 1/2*S.*sigma.^2 + mu_0*Ms*H1 - Y;
c2_m = eps_s.*sigma + 1/2*S.*sigma.^2 + Y - 2*k2_m.*eps_2./eps_th;
xi1 = (1./(2.*rho.*k1_m).*(eps_s*sigma+.5*S*sigma^2+mu_0.*Ms.*Hy_m-rho*c1-Y
+ K.*Hy_m));
gk = xi1>=abs(eps_s)/abs(eps_th);

```

C.7 Transducer Structure Matrix Generating Function

```

function [P_matrix,M] = strugen(vaTemp)
format long e %Scaled fixed point format with 15 digits.
%——-Enter desired number of elements
n = vaTemp(1); %Grid size: linked to r, see below. n=12*r.
%——-Rod geometry and grid characteristics.
L=vaTemp(2);
D=vaTemp(3); %rod diameter, meters
A=vaTemp(4); %cross-sectional area of rod
h=vaTemp(5); %grid step
%——-Initialize mass, stiffness and damping matrices.
M=zeros(n,n); K=M; C=M;
%——-Gaussian quadrature characteristics: c and x are weights and positions.
w=[0.34785484513745 0.65214515486255 0.6521451548625 0.34785484513745];
x=[-0.86113631159405 -0.33998104358486 0.33998104358486 0.86113631159405];
%——-Boundary terms.
% Kmps = 2.4e6; %Stiffness of prestress mechanism, N/m
K.L=vaTemp(6); %Stiffness of prestress mechanism, N/m
C.L=vaTemp(7); %Damping coefficient
m.L=vaTemp(8); %external load, kg
%——-Define material properties.
ro=vaTemp(9); %density, Terfenol-D
% E = 30e7; %Elastic modulus, Pa

```

```

E=vaTemp(10); %Elastic modulus, Pa
c_D=vaTemp(11); %Kelvin-Voigt damping coefficient
%——-Generation of system matrices: M, C, K and P_matrix.
f1=h/8*(1+x).^2;
f2=h/8*(1-x).^2;
g1=1/h;
for(i=1:n)
for(j=1:n)
if(i==j)
if(i ==n)
M(i,j)=ro*A*2*w*f1';
K(i,j)=E*A*2*g1;
C(i,j)=c_D*A*2*g1;
else
M(i,j)=ro*A*w*f1';
K(i,j)=E*A*g1;
C(i,j)=c_D*A*g1;
end
else
if(i==j+1 — j==i+1)
M(i,j)=ro*A*w*f2';
K(i,j)=-E*A*g1;
C(i,j)=-c_D*A*g1;
else
%M(i,j)=0;
end
end
end
end

M(n,n)=M(n,n)+m_L; %Add boundary term
K(n,n)=K(n,n)+K_L; %Add boundary term
C(n,n)=C(n,n)+C_L; %Add boundary term
P_matrix=[[zeros(n,n) eye(n,n)];[-inv(M)*K -inv(M)*C]];

```

C.8 Transducer Deformation Calculating Function

```

% Calculate the transducer deformation
clear all, clc
format long e %Scaled fixed point format with 15 digits.
tic

%=====
% START PROGRAM
%=====

n = 24; dc = 1;
E = 1.61e10;

% Rod geometry and grid characteristics.

```

```

L=0.02243; % rod length, meters
D=0.00635; % rod diameter, meters
A=pi*D^2/4; % cross-sectional area of rod
V=A*L;
% mass0 = 5.13e-3;
mass0 = 5.13e-3;
h=L/n; % grid size

% Select number of grid points and the loading
switch dc
case 1
    sigma = -0.0125e6;
    x = [1.1956, 1.0999, 0.78616, 0.031771];
case 2
    sigma = -0.13e6;
    x = [1, 0.53991, 1, 0.01];
case 3
    sigma = -0.27e6;
    x = [1, 0.92578, 0.8715, 0.010768];
case 4
    sigma = -0.41e6;
    x = [1, 1.6539, 0.73916, 0.01];
case 5
    sigma = -0.62e6;
case 6
    sigma = -1.79e6;
case 7
    sigma = -4.15e6;
end

loadforce = sigma*A;

% K, C, and m of external system
K_L = 2.4e7; %Stiffness, N/m
C_L = 0; %Damping coefficient
m_L=1; %external load, kg

% Define material properties.
ro = 7.981776029746337e+003; %density, Terfenol-D
c_D = 3e6; %Kelvin-Voigt damping coef

vaTemp = [n,L,D,A,h,K_L,C_L,m_L,ro,E,c_D];
[P_matrix,M] = strugen(vaTemp);

dt = 0.006; % delta t

%=====
% CONSTRUCT F_Matrix
%=====

[eps,H] = FEmodel_val(x,dc,'r');
Hlen = length(H);
f = zeros(n,Hlen);
for i =1:Hlen
    f(n,i) = E*A*eps(i)*1e-6 + loadforce; timeVec(i) = (i-1)*dt;
end

%=====

```

```
%ODESOLVER
```

```
%=====
```

```
Id_matrix = eye(2*n,2*n);
W_matrix = inv(Id_matrix-dt/2*P_matrix)*(Id_matrix+dt/2*P_matrix);
%%big W on page 552 2n*2n
F_matrix = dt/2*inv(Id_matrix-dt/2*P_matrix);
%%big F on page 552 2n*2n
Y_matrix = zeros(2*n,Hlen); %% deformation
% Using equation (23)
for(j=2:1:Hlen)
FV_j = zeros(2*n,1); FV_jm1 = zeros(2*n,1);
y_jm1 = zeros(2*n,1); y_j = zeros(2*n,1);
FV_j((n+1):2*n) = inv(M)*f(:,j);
FV_jm1((n+1):2*n) = inv(M)*f(:,j-1);
y_jm1 = Y_matrix(:,j-1);
y_j = W_matrix*y_jm1+F_matrix*(FV_j+FV_jm1);
Y_matrix(:,j) = y_j;
end
def_end = Y_matrix(n,:);
eps_end = (def_end/L)*1e6;
[eps_exp,H_exp] = dat_fun(dc);
toc
```

C.9 Parametric Efficiency Analysis Function

```
% K, C, and m of external system
Ke = 2.4e7; %Stiffness, N/m
Ce = 15e6; %Damping coefficient
me=.1; %external load, kg
sigma = -0.0125e6;
x = [1.1956, 1.0999, 0.78616, 0.031771];
% Parameters to solve the equation
n = 24;
dc = 1;
E = 7.7e9; % Youngs Modulus, from Adaptamat
miu0 = 4*pi*1e-7;
pm = 2.12e-8; % Piezomagnetic coefficient
% pm = 6e-8;
comp = 1/E; % Compliance
miur = 3;
miu = miur*miu0;
kapa = pm^2/(comp*miu);
ro = 7.981776029746337e+003; %density, NiMnGa
c_D = 3e6; %Kelvin-Voigt damping coef
c_D = 3e10; %Kelvin-Voigt damping coef
```

```

c_D = 3e4;
c_D = 0;
Inductance0 = 1;
% Rod geometry and grid characteristics.
L=0.02243; % rod length, meters
D=0.00635; % rod diameter, meters
A=pi*D^2/4; % cross-sectional area of rod
V=A*L;
% mass0 = 5.13e-3;
mass0 = 5.13e-3;
h=L/n; % grid size
loadforce = sigma*A;
[eps,H] = FEModel_val(x,dc,'r'); % Get the material deformation for the dynamic
test
Hlen = length(H);
f = zeros(n,Hlen);
dt = 0.0006; % dt
for i=1:Hlen
    f(n,i) = E*A*eps(i)*1e-6 + loadforce; timeVec(i) = (i-1)*dt;
end
Ki = E*A/L;
for i = 1:1000
    r(i) = 0.01*i;
    Ke = r(i)*Ki;
    vaTemp = [n,L,D,A,h,Ke,Ce,me,ro,E,c_D];
    [P_matrix,M] = strugen(vaTemp);
    %=====
    %ODESOLVER
    %=====

    Id_matrix = eye(2*n,2*n);
    W_matrix = inv(Id_matrix-dt/2*P_matrix)*(Id_matrix+dt/2*P_matrix);
    %%big W on page 552 2n*2n
    F_matrix = dt/2*inv(Id_matrix-dt/2*P_matrix);
    %%big F on page 552 2n*2n
    Y_matrix = zeros(2*n,Hlen); %% deformation
    % Using equation (23)
    for(j=2:Hlen)
        FV_j = zeros(2*n,1); FV_jm1 = zeros(2*n,1);
        y_jm1 = zeros(2*n,1); y_j = zeros(2*n,1);
        FV_j((n+1):2*n) = inv(M)*f(:,j);
        FV_jm1((n+1):2*n) = inv(M)*f(:,j-1);
        y_jm1 = Y_matrix(:,j-1);
        y_j = W_matrix*y_jm1+F_matrix*(FV_j+FV_jm1);
        Y_matrix(:,j) = y_j;
    end
end

```

```

def_end = Y_matrix(n,:);
eps_end = (def_end/L)*1e6;
% plot(H, eps_end);
mechenergytemp = 0;
elecenergytemp = 0;
Inductance(i) = Inductance0*(1-kapa*r(i)/(1+r(i)));
inputenergytemp = 0;
outputenergytemp = 0;
for j = 1:length(eps_end)/2
    mechenergytemp = mechenergytemp + Ke*(eps_end(j)*L)^2;
    elecenergytemp = elecenergytemp + Inductance(i)*(H(j))^2;

    inputenergytemp = inputenergytemp + Ki*(eps(j)*L)^2;
    outputenergytemp = outputenergytemp + r(i)*Ki*(eps_end(j)*L)^2;
end
mechenergy(i) = mechenergytemp;
elecenergy(i) = elecenergytemp;
inputenergy(i) = inputenergytemp;
outputenergy(i) = outputenergytemp;
end
for i = 1:length(r)
    eff(i) = kapa^2*r(i)/((1+r(i))^2*(1-kapa^2*r(i)/(1+r(i))));
end
figure(1)
hold on;
plot(r,eff)
axis([0 10 0 0.45])
xlabel('Stiffness ratio'); ylabel('Conversion efficiency from linear model');
convertingeffic = mechenergy./elecenergy;
figure(2)
hold on;
plot(r, eff, r,convertingeffic,'-')
% axis([0 10 0 0.45])
xlabel('Stiffness ratio');
% ylabel('Conversion efficiency from nonlinear model');
ylabel('Conversion efficiency')
legend('Linear model', 'Nonlinear model')
deliveryeffic = outputenergy./inputenergy;
figure(3)
hold on;
xlabel('Stiffness ratio'); ylabel('Delivery efficiency from nonlinear model');
axis([0 10 0 0.25])
plot(r,deliveryeffic);
% Calculate the delivery efficiency from linear model
for i = 1:1000
    r_d(i) = i*0.01;
    eff_dl(i) = r_d(i)/(1+r_d(i))^2;
end

```

```
figure(4)
hold on;
plot(r_d,eff_dl);
axis([0 10 0 0.25])
xlabel('Stiffness ratio'); ylabel('Delivery efficiency from linear model');
```

BIBLIOGRAPHY

- [1] G. Bertotti. “Space-time correlation properties of the magnetization process and eddy current losses: Applications. I. Fine wall spacing”. *Journal of Applied Physics*, 55(12):4339–4347, 1984.
- [2] G. Bertotti. “Space-time correlation properties of the magnetization process and eddy current losses: Applications. II. Large wall spacing”. *Journal of Applied Physics*, 55(12):4348–4355, 1984.
- [3] G. Bertotti. “Physical Interpretation of Eddy Current Losses in Ferromagnetic Materials. I. Theoretical Considerations”. *Journal of Applied Physics*, 57(6):2110–2117, 1985.
- [4] G. Bertotti. “Physical interpretation of eddy current losses in ferromagnetic materials. I. Theoretical considerations”. *Journal of Applied Physics*, 57(6):2110–2117, 1985.
- [5] G. Bertotti. “Physical interpretation of eddy current losses in ferromagnetic materials. II. Analysis of experimental results”. *Journal of Applied Physics*, 57(6):2118–2126, 1985.
- [6] G. Bertotti. “General properties of power losses in soft ferromagnetic materials”. *IEEE Transactions on Magnetics*, 24(1):621–630, 1998.
- [7] S. Brenner and R.L. Scott. *The mathematical theory of finite element methods*. Springer, 2005.
- [8] B. Carnahan, H.A. Luther, and J.O. Wikes. *Applied numerical methods*. Wiley, New York, 1969.
- [9] S. Chikazumi. *Physics of magnetism*. John Wiley, New York, 1964.
- [10] P.G. Ciarlet. *The finite element method for elliptic problems*. North-Holland, 1978.
- [11] B.D. Coleman and M.E. Gurtin. “Thermodynamics with internal state variables”. *The Journal of Chemical Physics*, 47(2):597–613, 1967.

- [12] B.D. Coleman and W. Noll. “The thermodynamics of elastic materials with heat conduction and viscosity”. *Archive for Rational Mechanics and Analysis*, 13(1):167–178, 1963.
- [13] COMSOL. *Structural mechanics: User’s guide*. COMSOL, 2007.
- [14] M.J. Dapino, R.C. Smith, and Flatau A.B. “Structural magnetic strain model for magnetostrictive transducers”. *IEEE Transactions on magnetics*, 36(3):545 – 556, May 2000.
- [15] A. Ern and J.L. Guermond. *Theory and practice of finite elements*. Springer, 2004.
- [16] L. Faidley. *Characterization and modeling of ferromagnetic shape memory NiMnGa in a collinear configuration*, Ph.D. Dissertation. Ohio State University, 2007.
- [17] L.E. Faidley, M.J. Dapino, and G.N. Washington. “Homogenized strain model for NiMnGa driven with collinear magnetic field and stress”. *Journal of Intelligent Material Systems and Structures*, 77:1273 – 1299, 1998.
- [18] L.E. Faidley, M.J. Dapino, G.N. Washington, and T. Lograsso. “Dynamic response in the low-kHz range and delta-E effect in ferromagnetic shape memory Ni-Mn-Ga”. *Proceedings of IMECE*, 43198:1273 – 1299, 2003.
- [19] E. Flint, C. Liang, and C.A. Rogers. “Electromechanical analysis of piezoelectric stack active member power consumption”. *Journal of Intelligent Material Systems and Structures*, 6(1):117–124, 1995.
- [20] V. Giurgiutiu and S.E. Lyshevski. *Micromechatronics: Modeling, Analysis, and Design with Matlab*. CRC Press, 2004.
- [21] V. Giurgiutiu and C.A. Rogers. “Power and energy capabilities of commercially-available induced-strain actuators under full-stroke dynamic conditions”. *Journal of Intelligent Material Systems and Structures*, 7(6):656–667, 1996.
- [22] V. Giurgiutiu and C.A. Rogers. “Power and energy characteristics of solid-state induced-strain actuators for static and dynamic applications”. *Journal of Intelligent Material Systems and Structures*, 8:738–750, 1997.
- [23] V. Giurgiutiu, C.A. Rogers, and R Chaudhry. “Energy-based comparison of solid-state induced-strain actuators”. *Journal of Intelligent Material Systems and Structures*, 7(1):4–14, 1996.

- [24] N.I. Glavatska, A.A. Rudenko, I.N. Glavatskiy, and L'vov V.A. "Statistical model of magnetostrain effect in martensite". *Journal of Magnetism and Magnetic Materials*, 265(2):142–151, 1998.
- [25] L. Hirsinger and C. Lexcellent. "Modeling detwinning of martensite platelets under magnetic and stress actions on Ni-Mn-Ga alloys". *Journal of Magnetism and Magnetic Materials*, 254.
- [26] L. Hirsinger and C. Lexcellent. "Internal variable model for magneto-mechanical behavior of ferromagnetic shape memory alloys Ni-Mn-Ga". *Journal of Physics IV France*, 112:977–980, 2003.
- [27] R.D. James and M. Wuttig. "Physics of condensed matter: structure, defects and mechanical properties". *Philosophical Magazine A*, 77:1273 – 1299, 1998.
- [28] D.C Jiles. *Introduction to magnetism and magnetic materials*. Chapman and Hall, 1991.
- [29] D.C Jiles. "Frequency dependence of hysteresis curves in "non-conducting" magnetic materials". *IEEE Transactions on Magnetics*, 29(6):3490–3492, 1993.
- [30] D.C Jiles. "Modeling the effects of eddy current losses on frequency dependent hysteresis in electrically conducting media". *IEEE Transactions on Magnetics*, 30(6):4326–4328, 1994.
- [31] B. Kiefer and D.C. Lagoudas. "Magnetic field-induced martensitic variant reorientation in magnetic shape memory alloys". *Philosophical Magazine*, 85(33).
- [32] B. Kiefer and D.C. Lagoudas. "Phenomenological modeling of ferromagnetic shape memory alloys". *Proceedings of SPIE Smart Structures and Materials, San Diego, CA*, 5387:164 – 176, 2004.
- [33] D.J. Leo. "Energy analysis of piezoelectric-actuated structures driven by linear amplifiers". *Journal of Intelligent Material Systems and Structures*, 10:36 – 45, 1999.
- [34] A.A. Likhachev. "Differential equation of hysteresis: Application to partial martensitic transformation in shape memory alloys". *Scripta Metallurgica et Materialia*, 32(4):633 – 636, 1995.
- [35] A.A. Likhachev, A. Sozinov, and K. Ullakko. "Different modeling concepts of magnetic shape memory and their comparison with some experimental results obtained in NiMnGa". *Materials Science and Engineering A*, 378:513–518, 2004.

- [36] A.A. Likhachev and K. Ullakko. “Magnetic-field-controlled twin boundaries motion and giant magneto-mechanical effects in NiMnGa shape memory alloy”. *Physics Letters A*, 275, 2000.
- [37] A.A. Likhachev and K. Ullakko. “Quantitative model of large magnetostrain effect in ferromagnetic shape memory alloys”. *The European Physical Journal B*, 14:263 – 267, 2000.
- [38] A. Malla. *Effect of composition on the magnetic and elastic properties of shape memory NiMnGa*. Master Thesis, 2003.
- [39] A. Malla, M. Dapino, T. Lograsso, and D. Schlager. “Large magnetically-induced strains in $\text{Ni}_{50}\text{Mn}_{28.7}\text{Ga}_{21.3}$ driven with collinear field and stress”. *Journal of Applied Physics*, 99(6), 2006.
- [40] L.E. Malvern. *Introduction to the mechanics of a continuous medium*. Prentice-Hall, Inc, 1969.
- [41] M.A. Marioni, S.M. Allen, and R.C. O’Handley. “Nonuniform twin-boundary motion in NiMnGa single crystals”. *Applied Physics Letters*, 84:4071–4073, 2004.
- [42] S.J. Murray, R.C. O’Handley, and S. Allen. “Model for discontinuous actuation of ferromagnetic shape memory alloy under stress”. *Journal of Applied Physics*, 89(2):1295 – 1301, 2001.
- [43] R.C. O’Handley. “Model for strain and magnetization in magnetic shape-memory alloys”. *Journal of Applied Physics*, 83(6):3263 – 3270, 1998.
- [44] R.C. O’Handley, S.J. Murray, M. Marioni, H. Nembach, and S.M. Allen. “Phenomenology of giant magneti-field-induced strain in ferromagnetic shape-memory materials”. *Journal of Applied Physics*, 87:4712 – 4717, 2000.
- [45] P.M. Prenter. *Splines and variational methods*. Wiley, New York, 1975.
- [46] R.L. Richard. *Systematic analysis of the crystal structure, chemical ordering, and microstructure of Ni-Mn-Ga ferromagnetic shape memory alloys*, Ph.D. Dissertation. Massachusetts Institute of Technology, Cambridge, MA, 2005.
- [47] N.N. Sarawate and M.J. Dapino. “A continuum thermodynamics model for the sensing effect in ferromagnetic shape memory NiMnGa”. *Journal of Applied Physics*, 101, 2007.
- [48] R. Smith. *Smart Material Systems : Model Development*. Society for Industrial and Applied Mathematics, Philadelphia, 2005.

- [49] R. Smith and J.E. Massad. *A unified methodology for modeling hysteresis in ferroelectric, ferromagnetic, and ferroelastic materials*. Technical Report CRSC-TR01-10, CRSC, 2001.
- [50] R.C. Smith, S. Seelecke, Z. Ounaies, and J. Smith. “A free energy model for hysteresis in ferroelectric materials”. *Journal of Intelligent Material Systems and Structures*, 14(11):719 – 739, 2003.
- [51] O. Soderberg, L. Straka, V. Novak, O. Heczko, S.P. Hannula, and V.K. Lindroos. “Tensile/Compressive behaviour of non-layered tetragonal NiMnGa alloy”. *Materials Science and Engineering A*, 386:27–33, 2004.
- [52] J. Stoer and Bulirsch R. *Introduction to numerical analysis*. Springer-Verlag, New York, 1980.
- [53] R. Tickle and R.D. James. “Magnetic and magnetomechanical properties of Ni₂MnGa”. *Journal of Magnetism and Magnetic Materials*, 195:627–638, 1999.